MAP7-driven cytoskeletal cross-talk establishes Sertoli cell polarity crucial for germ cell meiotic progression

Koji Kikuchi[1*], Toshihiko Fujimori[2], Mami Nakagawa[2], Keisuke Ohta[3], Ryuki Shimada[1], Sayoko Fujimura[4], Kei-ichiro Yasunaga[4], Shingo Usuki[4], Naoki Tani[4], Akira Nakamura[5], Kimi Araki[6], and Kei-ichiro Ishiguro[1]

[1]Department of Chromosome Biology, Institute of Molecular Embryology and Genetics, Kumamoto University, 2-2-1 Honjo, Chuo-ku, Kumamoto 860-0811, Japan

[2]Division of Embryology, National Institute for Basic Biology, 5-1 Higashiyama, Myodaiji, Okazaki, Aichi 444-8787, Japan

[3]Advanced Imaging Research Center, Kurume University School of Medicine, 67 Asahimachi, Kurume, Fukuoka 830-0011, Japan.

[4]Liaison Laboratory Research Promotion Center, Institute of Molecular Embryology and Genetics, Kumamoto University, 2-2-1 Honjo, Chuo-ku, Kumamoto 860-0811, Japan

[5]Department of Germline Development, Institute of Molecular Embryology and Genetics, Kumamoto University, 2-2-1 Honjo, Chuo-ku, Kumamoto 860-0811, Japan

[6]Institute of Resource Development and Analysis, Kumamoto University, 2-2-1 Honjo, Chuo-ku, Kumamoto 860-0811, Japan

***Corresponding author**: kojik@kumamoto-u.ac.jp (K.K.)

Abstract

Sertoli cells form a unique apical domain crucial for organizing the seminiferous epithelium and supporting germ cell development, though the underlying molecular mechanisms remain unclear. We identified MAP7, a microtubule-associated protein, as a key regulator of cytoskeletal integration essential for apical domain formation. MAP7 localizes to apical microtubules without overlapping stable, acetylated tubulin. Loss of MAP7 prevents lumen formation during the first wave of spermatogenesis due to disrupted apical domain architecture and ectopic expansion of tight junctions. Overall microtubule intensity remains largely unchanged in *Map7*-deficient Sertoli cells, but their organization is severely perturbed, indicating MAP7 facilitates dynamic remodeling for apical and epithelial organization. Proteomic analysis revealed that MAP7 forms a complex with non-muscle myosin II heavy chains MYH9 and MYH10. MYH9 normally concentrates at luminal regions where microtubules and F-actin converge, but in *Map7*-deficient cells it is diffusely distributed, indicating MAP7 mediates spatial integration of microtubules and actomyosin for localized remodeling. Single-cell RNA sequencing showed Sertoli cell differentiation largely persists without MAP7, whereas germ cells in *Map7*-deficient testes exhibit delayed meiotic progression, marked by expansion of pachytene subtypes. These findings establish MAP7 as a cytoskeletal integrator linking epithelial polarity to germline progression, providing insight into how tissue organization sustains fertility.

(200 words)

Introduction

Sertoli cells are highly specialized epithelial cells that serve as the architectural scaffold of the seminiferous epithelium and orchestrate spermatogenesis. Unlike classical columnar epithelia, Sertoli cells undergo a unique form of polarization during postnatal development, culminating in the formation of a distinct apical domain. This domain is essential for establishing the three-dimensional organization of the seminiferous tubules and generating a dynamic microenvironment that supports germ cell differentiation. As differentiating germ cells migrate from the basal to the luminal compartment, the Sertoli cell apical domain provides structural support and mediates localized delivery of trophic factors, adhesive interactions, and signaling cues required for maturation [1]. Disruption of apical architecture impairs germ cell development and causes male infertility, underscoring the physiological relevance of Sertoli cell polarity [2-5]. Although critical, the developmental timing and molecular mechanisms underlying Sertoli cell polarization and their relationship with apical domain formation remain poorly understood.

Sertoli cell polarity is established and maintained by dynamic cytoskeletal reorganization [6]. Actin filaments, key components of ectoplasmic specializations (ES), play a central role in cell-cell adhesion and junctional integrity among Sertoli cells and between Sertoli and germ cells [7, 8]. Basal ES includes actin-based adherens, and tight and gap junctions that contribute to the blood–testis barrier (BTB) and enable intercellular communication. Apical ES supports Sertoli–spermatid interactions critical for adhesion and maturation. Deletion of Sertoli-specific small GTPases, such as RAC1 and CDC42, which are key actin cytoskeleton regulators, disrupts apical ES formation and Sertoli cell polarity, causing spermatid differentiation defects and male infertility [4, 5]. Moreover, the role of the microtubule cytoskeleton in Sertoli cell polarization remains underexplored. Microtubules in Sertoli cells form bundles along the apical–basal axis and have been proposed to mediate intracellular transport and structural organization. Perturbations of microtubule organization, such as Sertoli cell-specific overexpression of the microtubule-nucleating protein γ-tubulin [9, 10] or expression of a dominant-negative form of the microtubule plus-end tracking protein EB1 [11], results in spermatogenic failure. Additionally, loss of the microtubule-severing enzyme KATNAL1 leads to disorganized microtubules and premature release of elongating spermatids [12]. These findings highlight an essential but poorly understood role of microtubule remodeling in Sertoli cell polarity and germ cell differentiation.

Microtubule dynamics are tightly regulated by various microtubule-associated proteins (MAPs) [13, 14]. Among them, the MAP7 family was a key microtubule regulator in cultured cells and *Drosophila*. This family includes four paralogs, namely MAP7, MAP7D1, MAP7D2, and

MAP7D3, containing an N-terminal microtubule-binding domain and a C-terminal kinesin-1–binding domain. These domains allow MAP7 proteins to stabilize microtubules and promote kinesin-1 loading, enabling intracellular transport [15-23]. MAP7 competes with other MAPs for microtubule binding, influencing motor protein distribution and activity in neurons [24, 25]. In HeLa cells, MAP7 and MAP7D1 cooperatively direct microtubule plus-ends to the cell cortex during migration and adhesion, independent of their microtubule stabilization and growth functions [18]. In mice, MAP7 is expressed in Sertoli and germ cells [26, 27]. Consistent with this, *Map7* gene-trap mutant mice show diminished microtubule bundle formation in Sertoli cells and structural defects in spermatid manchettes, suggesting that MAP7 is essential for microtubule organization [27]. However, it remains unclear whether MAP7 regulates dynamic microtubule remodeling during Sertoli cell polarization and contributes to germ cell development.

Microtubule remodeling plays an essential but poorly understood role in establishing Sertoli cell polarity and supporting germ cell differentiation. In this study, we aimed to elucidate the molecular mechanisms underlying apical domain formation in Sertoli cells during the first wave of spermatogenesis. We identified the microtubule-associated protein MAP7 as a central regulator of this process. MAP7 localizes to apical microtubules and promotes their dynamic remodeling, enabling spatial organization of cytoskeletal components essential for Sertoli cell polarity. Mechanistically, MAP7 forms a complex with non-muscle myosin II (NMII) heavy chains, MYH9 and MYH10, and directs MYH9 enrichment to luminal regions where microtubules and F-actin co-localize. In the absence of MAP7, MYH9 fails to accumulate apically and shows diffuse distribution, indicating that MAP7-mediated integration of microtubule and actomyosin networks is essential for localized cytoskeletal remodeling. Although single-cell RNA sequencing (scRNA-Seq) reveals that Sertoli cell differentiation programs are largely preserved without MAP7, their transcriptional trajectories are nonetheless disrupted. In contrast, MAP7-deficient testes exhibit delayed germ cell development, marked by expansion of pachytene subpopulations. These findings identify MAP7 as a key coordinator of cytoskeletal cross-talk required for apical domain formation and timely meiotic progression, linking epithelial polarity to spermatogenesis.

Results

Localization pattern of MAP7 in Sertoli cells

Map7 is expressed at the mRNA level in both Sertoli and male germ cells [26, 27]; however, its protein expression and subcellular localization remain uncharacterized. To investigate these aspects, we generated *Map7-egfp* knock-in (*Map7-egfp*^{KI}) mice (Extended Data Fig. 1a, b). To assess whether EGFP tagging affects MAP7 function, we confirmed the generation of homozygous mice and examined MAP7-EGFP^{KI} localization in the fallopian tubes, where we previously analyzed MAP7 expression using anti-MAP7 antibodies and *in vivo* electroporation of MAP7-EGFP [18]. *Map7-egfp*^{KI} mice were viable and fertile as homozygotes (Extended Data Fig. 1c). Consistent with prior findings, MAP7-EGFP^{KI} localized to the ovarian (proximal) side along the planar axis of multiciliated cells in the fallopian tubes (Extended Data Fig. 1d). Thus, our findings indicate that EGFP tagging does not disrupt MAP7 function in mouse tissues.

Next, we examined MAP7-EGFP^{KI} localization in adult testes by co-staining with TUBB3, a Sertoli cell-specific β-tubulin isoform. MAP7-EGFP^{KI} colocalized with Sertoli microtubules labeled with TUBB3 (Fig. 1a, top) and exhibited a polarized distribution toward the luminal side (Fig. 1a, top). This finding suggests the role of MAP7 in microtubule dynamics. Additionally, MAP7-EGFP^{KI} was expressed in step 9–11 spermatids, where phenotypes were observed in *Map7* gene-trap mice (Fig. 1a, bottom), and colocalized with acetylated tubulin, the manchette microtubule marker (Fig. 1b, bottom), indicating localization to manchette microtubules. However, MAP7-EGFP^{KI} did not colocalize with long-lived stable microtubules stained using acetylated tubulin, except in the manchette (Fig. 1b, top). These localization patterns in Sertoli cells and step 9–11 spermatids were further validated by immunostaining with an anti-MAP7 antibody (Fig. 1c). These findings demonstrate that MAP7 specifically localizes to apical microtubules in Sertoli cells and to manchette microtubules in step 9–11 spermatids, underscoring its potential role in microtubule dynamics during spermatogenesis.

MAP7 is essential for the establishment of Sertoli cell polarity and apical domain formation

Our analysis of MAP7 localization in Sertoli cells, along with phenotypes reported in *Map7* gene-trap mice, suggests a role for MAP7 in establishing Sertoli cell polarity. However, prior studies used *Map7* gene-trap mice on a mixed B6.129 background, and complete loss of MAP7 protein was not validated [27]. To directly assess the role of MAP7 in Sertoli cell polarity, we generated *Map7* knockout (KO) mice on a pure C57BL/6 background (Extended Data Fig. 2a–c). Complete loss of MAP7 protein in homozygous *Map7*$^{-/-}$ mice was confirmed using two

independent antibodies (Extended Data Fig. 2d). Heterozygous *Map7*$^{+/-}$ mice, which showed normal testis size and histology at 8 weeks (Extended Data Fig. 2e, f), were used as controls in subsequent analyses.

To delineate the temporal dynamics of Sertoli cell polarity establishment, we examined seminiferous tubule morphology during the first wave of spermatogenesis by analyzing cross-sections from postnatal day (P)10 to P35. By restricting our analysis to stages up to P23, prior to the emergence of step 9–11 spermatids, we effectively excluded potential contributions of MAP7 in germ cells, allowing us to specifically evaluate its role in Sertoli cells. In *Map7*$^{+/-}$ testes, seminiferous tubules were closed at P10, with early primary spermatocytes evident (Fig. 2a, b; Extended Data Fig. 3). By P15, lumina were present in 13.2% of tubules, increasing to 81.2% by P17, coinciding with the appearance of pachytene spermatocytes. By P21, lumina were detected in 96.7% of tubules and became nearly ubiquitous thereafter (Fig. 2a, b; Extended Data Fig. 3). These findings are consistent with prior reports that Sertoli cell polarization and BTB formation begin around P15–P17, concurrent with pachytene spermatocyte development [28, 29]. The results indicate that Sertoli cells complete polarity establishment by P21. In contrast, *Map7*$^{-/-}$ tubules appeared morphologically normal at P10 but failed to form lumina between P15 and P28. By P35, multi-lumen structures or abnormally formed lumina were observed (Fig. 2a, b; Extended Data Fig. 3). These observations demonstrate that MAP7 is essential for seminiferous tubule remodeling and implicate it in apical domain formation during Sertoli cell polarization.

Directly assessing Sertoli cell adhesion and morphology is challenging due to the intimate association between Sertoli and germ cells within the seminiferous epithelium. To overcome this, we used serial sectioning and scanning electron microscopy (SEM). In P10 *Map7*$^{+/-}$ mice, 89.3% (25/28) of Sertoli cells adhered to the basement membrane, but only 60.7% (17/28) of Sertoli nuclei were positioned basally (Fig. 2c). By P21, all Sertoli cells adhered (12/12), and 91.7% (11/12) of their nuclei were basal (Fig. 2c). To quantify nuclear positioning in a larger cohort, we performed SOX9 immunostaining. The results showed a similar trend, with basal nuclei increasing to 80.5% from P10 to P17 (Fig. 2d, e; Extended Data Fig. 4a). These findings suggest that at P10, many Sertoli cells exhibit incomplete apical–basal compartmentalization, which progressively matures. Consistent with progressive polarization and lumen formation, Sertoli cells adhering to the basement membrane underwent distinct morphological changes over time (Fig. 2c). In transverse views, Sertoli cells extended apically from P10 to P21 (Fig. 2c) and elongated along the longitudinal axis, suggesting that Sertoli cell polarity is established along both apical–basal and longitudinal axes during development. In

Map7$^{-/-}$ mice, Sertoli cell adhesion and nuclear positioning were markedly impaired (Fig. 2c–e; Extended Data Fig. 4a). At P10, 59.5% (22/37) of Sertoli cells adhered to the basement membrane, and only 54.1% (20/37) of their nuclei were basal. By P21, adhesion further decreased, with only 31.6% (6/19) of Sertoli cells attached and 26.3% (5/19) of nuclei basally positioned (Fig. 2c). SOX9 immunostaining revealed a similar trend: the proportion of basal nuclei was 24.9% at P10 and declined to 18.2% at P17 (Fig. 2d, e; Extended Data Fig. 4a), indicating failed apical–basal compartmentalization in *Map7*$^{-/-}$ Sertoli cells. This defect persisted into adulthood (Extended Data Fig. 4b, c). Additionally, in P21 *Map7*$^{-/-}$ mice, Sertoli cells that adhered to the basement membrane failed to elongate in either axis, and apical extension was absent (Fig. 2c), reflecting severe loss of polarity and apical domain formation. In P10 *Map7*$^{+/-}$ mice, luminal F-actin signals were detected but disappeared by P17, coinciding with lumen formation (Fig. 2d; Extended Data Fig. 4a). In contrast, in *Map7*$^{-/-}$ mice, luminal F-actin signals persisted at P17, consistent with histological evidence of closed lumina (Fig. 2d; Extended Data Fig. 4a). These findings suggest that MAP7 is required for actin cytoskeletal remodeling during apical domain formation.

Sertoli cells and male germ cell lineages interact closely within the seminiferous tubules [30-34]. To determine whether MAP7 regulates Sertoli cell polarity in a male germ cell lineage-dependent or -independent manner, we examined Sertoli cell nuclear orientation after busulfan-induced depletion of spermatogonial stem cells (SSCs). Following treatment, *Map7*$^{+/-}$ mice showed testis-to-body weight ratios similar to untreated *Map7*$^{-/-}$ mice, and hematoxylin-eosin (HE) staining confirmed germ cell depletion (Extended Data Fig. 5a, b). In *Map7*$^{+/-}$ mice, most Sertoli nuclei were basal, whereas in *Map7*$^{-/-}$ mice, Sertoli nuclei were frequently oriented toward the lumen (Fig. 2f; Extended Data Fig. 5b). These data indicate that MAP7 regulates Sertoli cell polarity independently of germ cell presence.

Collectively, these results demonstrate that MAP7 is indispensable for the establishment of Sertoli cell polarity and apical domain formation. Loss of MAP7 disrupts cytoskeletal remodeling, nuclear positioning, and cell elongation, impairing lumen formation and seminiferous tubule architecture.

MAP7 facilitates microtubule remodeling, but not microtubule stabilization, to establish Sertoli apical domain

Our analysis showed that Sertoli cells attach to the basement membrane and establish polarity between P10 and P21, a process dependent on MAP7. To investigate cytoskeletal remodeling and MAP7 localization during polarization, we examined two major cytoskeletal

components—microtubules and actin filaments at P10 (before polarization) and P17 (onset of polarization). At P10, microtubules, actin filaments, and MAP7-EGFP^{KI} accumulated on the inner side of the seminiferous tubules and extended toward the basement membrane (Fig. 3a, top). By P17, these inner cytoskeletal components disappeared. Microtubules aligned along the luminal–basal axis, and actin filaments reorganized into the basal ES near the basement membrane (Fig. 3a, bottom). Consistent with observations in adult testes (Fig. 1a, c), MAP7 exhibited polarized distribution along microtubules, becoming enriched toward the luminal side (Fig. 3a, bottom). These results indicate that cytoskeletal remodeling, including luminal MAP7 accumulation, occurs after P10 as Sertoli cells establish polarity.

We next examined the impact of *Map7* deletion on cytoskeletal remodeling during Sertoli cell polarization. Previous studies reported reduced microtubule bundles in Sertoli cells of *Map7* gene-trap mice at P21 [27]. As shown above, Sertoli microtubules undergo extensive reorganization between P10 and P17 (Fig. 3a). In *Map7*$^{+/-}$ mice, microtubules on the inner side of the tubules, which were prominent at P10, were lost by P17 (Fig. 3b). In contrast, in *Map7*$^{-/-}$ mice, inner microtubule signals persisted at P17, resembling the P10 pattern in wild-type and *Map7*$^{+/-}$ mice (Fig. 3a, top; Fig. 3b, bottom). Although actin filaments relocated to form the basal ES by P17 in control mice (Fig. 3a, bottom; Fig. 3b, top), they remained abnormally accumulated on the luminal side in *Map7*$^{-/-}$ mice (Fig. 3b, bottom). These findings suggest that Sertoli cells fail to transition beyond a P10-like cytoskeletal organization in the absence of MAP7, indicating the importance of MAP7 in cytoskeletal remodeling during polarization.

In *Map7*$^{+/-}$ mice, Sertoli microtubules extended along the luminal–basal axis (Extended Data Fig. 5a, top). In *Map7*$^{-/-}$ mice, although microtubule staining intensity was preserved, alignment was disrupted (Extended Data Fig. 5a, bottom). Similarly, actin filaments forming the apical ES were present in *Map7*$^{+/-}$ testes but replaced by ectopic actin structures in *Map7*$^{-/-}$ mice (Extended Data Fig. 5a, bottom). These results suggest that MAP7 promotes microtubule alignment rather than stabilization, thereby organizing the cytoskeletal framework.

Since cytoskeletal organization is essential for apical domain formation, we examined whether MAP7 is required for the assembly of Sertoli cell junctional structures. In the testis, tight junctions reside at the basal side of Sertoli cells and contribute to BTB formation, partitioning the seminiferous epithelium into basal and luminal compartments. We then performed SEM to assess the effect of *Map7* KO. In P21 *Map7*$^{+/-}$ testes, electron-dense regions near the basement membrane corresponded to tight junctions closely associated with endoplasmic reticulum at Sertoli–Sertoli interfaces, consistent with previous reports [35] (Fig. 3c; Extended Data Fig. 5b). Adherens junctions were observed apical to the tight junctions and

associated with endoplasmic reticulum. These structures were absent in both P10 *Map7*$^{+/-}$ and *Map7*$^{-/-}$ testes (Fig. 3c; Extended Data Fig. 5b). In P21 *Map7*$^{-/-}$ mice, Sertoli cells formed expanded basal tight junctions but lacked adherens junctions (Fig. 3c; Extended Data Fig. 5b). Consistent with these ultrastructural findings, ZO-1, a tight junction marker, localized specifically to the basal ES, marked by F-actin, in *Map7*$^{+/-}$ testes (Fig. 3d; Extended Data Fig. 5c). In *Map7*$^{-/-}$ testes, ZO-1 mislocalized to ectopic F-actin-rich regions (Fig. 3d; Extended Data Fig. 5c). β-catenin, a core adherens junction component, colocalized with F-actin at junctional regions near the basal ES in *Map7*$^{+/-}$ testes (Fig. 3b; Extended Data Fig. 5a). In *Map7*$^{-/-}$ testes, β-catenin accumulated on the luminal side, reflecting mislocalization of actin and microtubules (Fig. 3b; Extended Data Fig. 5a). Together, these results show that MAP7-dependent microtubule remodeling coordinates cytoskeletal architecture and junctional complex assembly, enabling apical domain formation during Sertoli cell polarization.

MAP7 mediates cytoskeletal cross-talk by forming a complex with actomyosin components

MAP7 promotes microtubule remodeling during Sertoli cell polarization, potentially by orchestrating broader cytoskeletal reorganization. To elucidate the molecular basis of this activity, we identified MAP7-interacting proteins using comparative immunoprecipitation-mass spectrometry (IP-MS). We analyzed two datasets: one from *MAP7-egfp*^{KI} HeLa cells (Fig. 4a) and another from testes of P17–P20 *Map7-egfp*^{KI} mice (Fig. 4b). The kinesin-1 heavy chain KIF5B, a known MAP7 interactor, was detected in both datasets, validating the robustness of our IP-MS approach. Comparative analysis identified 22 proteins that specifically co-immunoprecipitated with MAP7 in P17–P20 testes (Fig. 4c). Functional enrichment analysis via Metascape revealed significant overrepresentation of categories, such as motor proteins and Rho GTPase effectors (Fig. 4d). Based on these categories, we focused on cytoskeletal regulators among the 22 candidates (Fig. 4e), including TUBB3, NMII heavy chains MYH9 and MYH10, and vimentin (VIM), a key intermediate filament protein.

We prioritized MYH9 for further study due to its strong enrichment and established role in cytoskeletal remodeling. We examined MYH9 localization during Sertoli cell polarization and its dependence on MAP7. MYH9 was selectively enriched at luminal regions where microtubules and F-actin co-localized but was absent from areas lacking either component (Fig. 4f). In *Map7*$^{-/-}$ testes, microtubule and F-actin structures persisted in luminal regions where they are typically cleared during polarization; however, MYH9 failed to localize to these ectopic domains and instead remained diffusely distributed in the cytoplasm (Fig. 4f). These findings suggest that MAP7 facilitates spatial integration of microtubules and F-actin

through its interaction with NMII heavy chains, enabling localized actomyosin recruitment and cytoskeletal remodeling at the luminal interface of Sertoli cells.

Functional differentiation of Sertoli cells is largely preserved in the absence of MAP7

We showed that MAP7-mediated cytoskeletal remodeling establishes the Sertoli apical domain, which forms a structural scaffold for seminiferous epithelium organization. We performed scRNA-Seq at P19 to determine whether loss of MAP7 affects functional differentiation of Sertoli cells. GFP-positive Sertoli cells were isolated using a *Sox9-ires-gfp* allele combined with fluorescence-activated cell sorting (FACS) (Extended Data Fig. 5a). Germ cell contamination was detected despite efficient dissociation and library construction using the 10x Genomics platform. Hence, Sertoli cell-specific transcriptomes were extracted based on *Gata4*, *Sox9*, *Kitl*, and *Dhh* expression, yielding 311 wild-type and 434 *Map7*$^{-/-}$ cells (Extended Data Fig. 5b).

UMAP clustering identified six distinct clusters (C0–C5) (Fig. 5a). Gene enrichment analysis using Metascape analysis revealed functional specialization within each cluster (Fig. 5b; Extended Data Fig. 6). Cluster C0 was enriched for genes involved in responses to chemical stress, delineating a subtype equipped for multifaceted protection against oxidative and metabolic stressors through coordinated regulation of metabolic activity, mitochondrial function, proteostasis, cytoskeletal integrity, and gene regulation. C1 showed upregulation of fructose metabolism–related genes, suggesting a metabolically active population with enhanced mitochondrial and antioxidant function. Cluster C2 expressed genes involved in establishing and maintaining cell polarity, representing a dynamic population responsive to cues within the spermatogenic niche. C3 was enriched for genes responsive to cytoskeletal dynamics and TGFβ signaling, implicating it in extracellular matrix (ECM) remodeling, growth factor signaling, and cell proliferation control. C4 expressed ECM-related genes, indicating a structurally specialized subtype involved in ECM synthesis and BTB maintenance. C5 showed co-upregulation of stress response and carbon metabolism genes, suggesting a high-energy, stress-adapted state supporting spermatogenesis via mitochondrial activity, antioxidant defense, and protein homeostasis mechanisms. To assess relationships among clusters, we calculated pairwise Spearman correlation coefficients and visualized transcriptional trajectories using a minimum spanning tree (MST) (Fig. 5c). In wild-type cells, C1 occupied the root of the MST, consistent with its plastic, metabolically active profile. Two major differentiation paths emerged: one extending from C1 to C3, then C4, and another from C1 to C0, then bifurcating toward C2 or C5. In *Map7*$^{-/-}$ Sertoli cells, C1 remained at the root, but transcriptional distances between C1 and C0, C2, and C3 were reduced, suggesting a rearranged differentiation topology. Notably, C2

branched directly from C1, bypassing C0. *Map7*$^{-/-}$ Sertoli cells showed a modest but significant increase in C1, whereas C0 was reduced and C2 was elevated (Fig. 5d). The C5 fraction, which emerges downstream of C0, was also reduced, likely reflecting C0 depletion. These data indicate that loss of MAP7 subtly alters Sertoli cell differentiation architecture without inducing aberrant subtypes. Thus, functional differentiation of Sertoli cells is largely preserved in the absence of MAP7.

Sertoli apical domain ensures orderly progression through the pachytene stage during meiosis

Our analyses showed that MAP7 coordinates the remodeling of microtubule and actin networks and regulates the formation of junctional structures. While MAP7 is essential for apical domain formation and its disruption alters specific aspects of Sertoli cell function, the overall functional differentiation of Sertoli cells is largely preserved in its absence. Sertoli cell adhesion generates the stem cell niche for SSCs [36, 37]. To assess this further, we quantified SSCs in 8-week-old *Map7*$^{+/-}$ and *Map7*$^{-/-}$ mice. GFRα1^{+} SSCs were not reduced in *Map7*$^{-/-}$ mice compared to those in *Map7*$^{+/-}$ controls (Fig. 6a, b), suggesting that Sertoli cells can still support the SSC niche despite the loss of adherens junctions, gap junctions, and apical domain, provided tight junctions are present. We next examined spermatogenic progression in 8-week-old *Map7*$^{+/-}$ and *Map7*$^{-/-}$ mice using ZFP541, a marker expressed from pachytene spermatocytes to round spermatids. Cell populations were quantified based on nuclear morphology and SYCP3 co-expression. In *Map7*$^{-/-}$ testes, both pachytene spermatocytes and round spermatids were reduced, with a more pronounced decrease in round spermatids (Fig. 6c, d; Extended Data Fig. 7a). To determine whether this reduction was due to increased cell death, we performed TUNEL staining. No apoptotic cells were observable in either genotype (Extended Data Fig. 7b), indicating that round spermatid reduction cannot be attributable to cell death but instead suggests delayed differentiation into the round spermatid stage.

To assess the impact of apical domain disruption on germ cell development, we performed scRNA-Seq at P23, a stage preceding the appearance of step 9–11 spermatids (Extended Data Fig. 7c). This timing enabled focused analysis on earlier spermatogenic populations. At this stage, phenotypes observed in *Map7*$^{-/-}$ testes, including luminal closure, abnormal microtubule organization, and ectopic accumulation of F-actin and β-catenin, remained evident (Extended Data Fig. 7c, d). We dissociated whole testes from *Map7*$^{+/-}$ and *Map7*$^{-/-}$ mice and performed scRNA-Seq using the 10x Genomics platform. Germ cells were identified by *Ddx4* expression, yielding 1,914 *Map7*$^{+/-}$ and 4,745 *Map7*$^{-/-}$ germ cells (Extended

Data Fig. 8). After dataset integration and unsupervised clustering, we identified 15 clusters (clusters 0–14; Extended Data Fig. 9a). To define germ cell differentiation stages, we used stage-specific marker analysis and RNA velocity profiling (Extended Data Fig. 9b, c). Metascape analysis revealed distinct biological processes enriched in each cluster, aligned with the expected progression of spermatogenesis (Extended Data Fig. 10). Based on inferred trajectory positions, clusters were renamed Ca–Co to reflect their differentiation order (Fig. 6e; Extended Data Fig. 9a). We then quantified the proportion of cells in each cluster to assess genotype-specific changes. To determine whether cluster expansion reflected aberrant meiotic entry, we examined expression of *Stra8* and *Meiosin*, key meiotic inducers [38]. Both genes were appropriately upregulated at meiotic entry and downregulated thereafter in *Map7*$^{-/-}$ germ cells, consistent with *Map7*$^{+/-}$ controls (Extended Data Fig. 11a). STRA8 protein levels were similarly unchanged between genotypes (Extended Data Fig. 11b), indicating that meiotic initiation and early transcriptional programs remained intact. Despite appropriate meiotic entry, cytological assessment showed delayed progression in *Map7*$^{-/-}$ testes, with significantly fewer seminiferous tubules containing round spermatids compared to *Map7*$^{+/-}$ controls (Extended Data Fig. 11c, d). To clarify the identity of expanded clusters Cg and Ci in *Map7*$^{-/-}$ testes, we analyzed the expression of *Prelid1* and *Ccna1*, which mark early and late pachytene stages, respectively. *Prelid1* is expressed through early pachytene, and its downregulation marks the transition to mid-pachytene [39], whereas *Ccna1* expression increases during late pachytene and remains high into diplotene [40]. *Prelid1* expression extended through Cg, indicating that Cg represents early pachytene cells expanded in *Map7*$^{-/-}$ testes (Fig. 6g). *Ccna1* was elevated in Ci of *Map7*$^{-/-}$ testes, whereas in *Map7*$^{+/-}$ testes, it was restricted to Cj, identifying Ci as a late pachytene population unique to *Map7*$^{-/-}$ mice. Notably, trajectory inference indicated that the Ci cluster in *Map7*$^{-/-}$ testes progresses to Ck (diplotene) through an alternative route that bypasses the Cj stage, as observed in *Map7*$^{+/-}$ mice (Fig. 6g). Together, these findings demonstrate that the Sertoli apical domain is essential for guiding orderly progression through the pachytene stage of meiosis.

Discussion

We identified MAP7 as a key regulator of Sertoli cell polarity and apical domain formation, revealing a previously unrecognized molecular nexus that integrates microtubule dynamics with cytoskeletal cross-talk to support spermatogenesis. Although the importance of Sertoli cell polarization in testicular architecture and germ cell development is well established [1], the molecular mechanisms underlying microtubule remodeling in this context have remained poorly defined. We showed that MAP7 is enriched at apical microtubules in Sertoli cells, where it orchestrates microtubule remodeling, a function distinct from stabilization, to support polarity. This remodeling is essential for the spatial coordination of F-actin, mediated in part through complexes involving NMII heavy chains (MYH9 and MYH10). Our biochemical analyses demonstrate that MAP7 forms complexes with MYH9/10, supporting a model in which MAP7 acts as a scaffold bridging microtubules and the actomyosin cytoskeleton. Disruption of this network in *Map7*$^{-/-}$ Sertoli cells leads to impaired cytoskeletal coordination, abnormal morphology, selective loss of junctional structures (excluding tight junctions), and failure of lumen formation.

We further showed that MYH9 is enriched at luminal regions where microtubules and F-actin co-localize—a pattern lost in *Map7*$^{-/-}$ Sertoli cells. Notably, MYH9 fails to accumulate even at ectopic sites where microtubules and F-actin are present, indicating that MAP7-mediated integration is required for NMII localization. This spatial regulation resembles NMII behavior in other epithelia. In the nephric duct and ureteric bud, NMII accumulates apically to support constriction and E-cadherin–mediated adhesion [41]. Similarly, in dental epithelium, apical MYH9 facilitates convergent cell movement and stable adhesion for invagination [42]. Analogously, MAP7-dependent scaffolding in Sertoli cells recruits MYH9/10 to the apical domain, enabling F-actin remodeling and robust junction formation. The inability of *Map7*$^{-/-}$ Sertoli cells to recruit MYH9 despite intact microtubules and F-actin suggests that MAP7 not only scaffolds these elements but also creates a microenvironment encouraging NMII complex assembly and activity.

Our findings extend previous work implicating actin regulators, such as RAC1 and CDC42, in Sertoli cell polarity by highlighting microtubule remodeling as a complementary and indispensable mechanism [4, 5]. Unlike previous studies that focused on actin dynamics, our identification of MAP7-driven microtubule remodeling as a key driver of Sertoli apical domain formation reveals an essential aspect of cytoskeletal integration in epithelial organization. In *Map7*$^{-/-}$ Sertoli cells, adherens and gap junctions are disrupted, whereas tight junctions are abnormally expanded, indicating imbalanced junctional composition and spatial organization.

Although we did not directly assess BTB permeability, the loss of adhesion and communication junctions, both critical to BTB function, suggests that MAP7 deficiency may compromise its integrity. As BTB assembly depends on coordinated localization of multiple junction types, mislocalization of tight junctions alone is unlikely to preserve barrier function. Thus, MAP7 appears essential for establishing the structural foundation of a functional BTB, though further studies are needed to define the extent of impairment.

Sertoli cells form the SSC niche through BTB construction and secretion of trophic factors that support SSC maintenance and differentiation [36, 37]. Sertoli cell polarity determines the spatial organization of junctions and shapes the microenvironment required for germ cell development. Although polarity loss has been linked to impaired niche function, our data showed that in *Map7*$^{-/-}$ Sertoli cells, tight junctions are retained but ectopically formed, whereas adherens junctions fail to assemble. Despite these abnormalities, SSC numbers remain unchanged throughout the eight weeks, and the first wave of spermatogenesis proceeds without overt defects in spermatogonial differentiation. These findings suggest that tight junctions (even when mislocalized) may be sufficient to support early spermatogenesis, and that canonical apical domain architecture is not essential for SSC maintenance during the postnatal period.

Our scRNA-Seq analyses showed that despite severe defects in polarity and apical domain formation, the intrinsic transcriptional differentiation programs of Sertoli cells are largely maintained in *Map7*$^{-/-}$ mice. This suggests that MAP7 primarily influences spatial and structural organization rather than core cellular identity. Thus, Sertoli apical domain architecture may govern the germ cell niche through spatial rather than transcriptional regulation, explaining the delayed meiotic progression observed in *Map7*-deficient testes. This delay occurs in the absence of increased apoptosis or defects in meiotic initiation, implicating the apical domain as a critical structural niche component that ensures timely progression through meiosis. Given the reliance of germ cells on Sertoli-derived structural and trophic support, our data suggest that microtubule-driven apical remodeling orchestrates key intercellular interactions required for germ cell differentiation.

In summary, MAP7 is a master regulator of Sertoli cell polarity that promotes seminiferous tubule morphogenesis and spermatogenic progression through microtubule remodeling and cytoskeletal coordination. By forming complexes with MYH9/10, MAP7 facilitates cytoskeletal cross-talk essential for epithelial polarization. Although this mechanism may reflect a broader principle of epithelial organization, Sertoli cells possess distinctive polarity features and junctional architectures not found in typical columnar epithelia. Consistent with this, loss of the MAP7 homolog Ensconsin in *Drosophila* disrupts planar cell polarity

without affecting apico-basal polarity [18], suggesting that MAP7-dependent scaffolding functions are highly context-dependent and may govern different aspects of epithelial organization depending on cell type. Despite these insights, our study has several limitations. First, although we demonstrated the role of MAP7 in Sertoli cell polarity and junctional organization using mouse models, it remains unclear whether this mechanism is conserved across other mammalian epithelia. Given the specialized architecture of Sertoli cells and prior evidence of context-dependent MAP7 function in invertebrate systems, further studies are required to assess the generality of these findings. Second, although we characterized Sertoli cell polarization in fixed tissues, real-time analysis at ultrastructural resolution remains highly challenging due to the dense packing and complex morphology of Sertoli cells. To overcome these difficulties, we employed SEM-based array tomography to reconstruct individual cell architecture (Fig. 2c). However, achieving comparable resolution in live imaging—particularly without mosaic labeling to clearly delineate single cells within this crowded environment—remains a formidable technical barrier. Overcoming this limitation is essential to fully elucidate MAP7's dynamic role in polarity establishment. Finally, while we evaluated the impact of MAP7 loss on Sertoli cell architecture and early germ cell development, the long-term consequences for fertility, BTB integrity, and testicular homeostasis remain unknown. Future studies incorporating live imaging, temporally controlled gene perturbation, and cross-epithelial comparisons will be critical to fully define the roles of MAP7 in epithelial polarity and its relevance to reproductive and barrier-related disorders.

Materials and Methods

Animals

We used *Map7*$^{+/-}$, *Sox9-ires-gfp;Map7*$^{+/-}$, and *Map7-egfp*^{KI} mice, all maintained on a C57BL/6 background, for this study. The *Sox9-ires-gfp* mouse line was originally generated by Nel-Themaat *et al*. [43]. For scRNA-Seq of total testis cells, *Map7*$^{+/-}$ or *Map7*$^{-/-}$ male mice at P23 were used. For scRNA-Seq targeting Sertoli cells, *Sox9-ires-gfp* or *Sox9-ires-gfp; Map7*$^{-/-}$ male mice at P19 were used. Testes collected from mice at P10–P35 and at eight weeks of age were used for histological and immunostaining analyses. Whenever possible, KO animals were compared with littermates or age-matched non-littermate controls from the same colony, unless otherwise specified. Mice were housed under standard conditions in a temperature- and light-controlled facility (12-hour light/dark cycle; 22 ± 1 °C). All animal procedures were approved by the Institutional Animal Care and Use Committee (approval numbers: A2019-127, A2021-018, A2023-036, and A2025-018) and conducted in accordance with institutional guidelines.

Cell culture

Wild-type and *MAP7-EGFP*^{KI} HeLa cells were cultured in Dulbecco's Modified Eagle Medium (DMEM; Fujifilm Wako Pure Chemical, Osaka, Japan) supplemented with 10% fetal bovine serum (FBS) and penicillin–streptomycin at 37 °C in a humidified atmosphere containing 5% CO [18].

Generation of *Map7*$^{+/-}$ mice and genotyping

Map7$^{+/-}$ mice were generated by introducing Cas9 protein (317-08441; NIPPON GENE, Toyama, Japan), tracrRNA (GE-002; FASMAC, Kanagawa, Japan), and synthetic crRNA (FASMAC) into C57BL/6N fertilized eggs via electroporation. To generate the *Map7* exon2–8 deletion (Ex2-8Δ) allele, synthetic crRNAs were designed to target the sequences GGACAAACTAGCAACCACTC(AGG) in exon 2 and CGCCTGAGGGCTCTGCACGA(AGG) in exon 8 of the *Map7* gene.

The electroporation mixture consisted of tracrRNA (10 μM), synthetic crRNA (10 μM), and Cas9 protein (0.1 μg/μL) in Opti-MEM I Reduced Serum Medium (31985062; Thermo Fisher Scientific, Waltham, MA, USA). Electroporation was performed using the Super Electroporator NEPA 21 (NEPA GENE, Chiba, Japan) on glass microslides with round wire electrodes (1.0 mm gap, 45-0104; BTX, Holliston, MA, USA). The procedure included four

steps of square-wave pulses: (1) three poring pulses of 3 ms each at 30 V with 97 ms intervals; (2) three polarity-reversed poring pulses of 3 ms each at 30 V with 97 ms intervals; (3) five transfer pulses of 50 ms each at 4 V with 50 ms intervals and 40% decay in voltage per pulse; and (4) five polarity-reversed transfer pulses of 50 ms each at 4 V with 50 ms intervals and 40% decay in voltage per pulse.

The targeted *Map7* Ex2-8Δ allele in F0 mice was identified via PCR using the following primers: *Map7*_C1F (5′-TAATGCAGGACCAGTCACTCTGCTGAACAG-3′) and *Map7*_C2R (5′-CTGTCACCTGATCTTGTACCCA-3′) for the KO allele (366 bp); *Map7*_C1F and *Map7*_C1R (5′-TAAGAACAGTAACTGCCCTTGCAGAGGACC-3′) for the exon 2 of the wild-type allele (597 bp); or Map7_C2F (5′-ACCTGCACTCTAGTTATCCCCA-3′) and *Map7*_C2R for the exon 8 of the wild-type allele (228 bp). PCR amplicons were confirmed using Sanger sequencing.

Generation of *Map7-egfp* knock-in mice and genotyping

Map7-egfp^{KI} mice were generated using the PITCh system, as previously described [44]. Cas9 protein, tracrRNA, synthetic crRNA, and the PITCh vector were introduced into C57BL/6N fertilized eggs via electroporation. The synthetic crRNA was designed to target the sequence ACTCATATAACTTCTACATG(AGG) within the Map7 gene and GTGCTTCGATATCGATCGTT(TGG) within the PITCh vector.

The targeted *Map7-egfp*^{KI} allele in F0 mice was identified by PCR using the following primers: *Map7-egfp*_C1F (5′-CTGACCTGTTCTTCCTACAGCA-3′) and *Map7-egfp*_C1R (5′-AGCCTGAAGTTCCATTCATTGT-3′) to amplify both the *Map7-egfp*^{KI} allele (996 bp) and the wild-type allele (228 bp). To confirm 5′ integration of the *Map7-egfp*^{KI} allele, primers *Map7-egfp*_C1F and *Map7-egfp*_E1R (5′-TTGTACAGCTCGTCCATGCCGAG-3′) were used to amplify a 935 bp fragment; for 3′ integration, *Map7-egfp*_E1F (5′-ACCACATGAAGCAGCACGACTTC-3′) and *Map7-egfp*_C1R were used to amplify a 548 bp fragment. All PCR amplicons were confirmed by sequencing.

Immunoblotting

For immunoblotting, testes were lysed in Laemmli sample buffer. After boiling, the lysates were separated by SDS–PAGE, transferred to polyvinylidene difluoride (PVDF) membranes (MilliporeSigma, Burlington, MA, USA), and immunoblotted with antibodies.

Histological analysis

For HE staining, testes and epididymides were fixed in 10% neutral buffered formalin or Bouin's solution, followed by paraffin embedding. Sections were cut at a thickness of 6 μm and mounted on CREST-coated glass slides (Matsunami Glass, Osaka, Japan). After dehydration, sections were stained with HE using standard protocols.

For immunofluorescence, testes were fixed overnight at 4 °C in 4% paraformaldehyde in PBS, then cryoprotected by immersion in 10%, 20%, and 30% sucrose solutions at 4 °C. Tissues were briefly incubated in OCT compound (Sakura Finetechnical, Tokyo, Japan) at room temperature, embedded in OCT, and snap-frozen in liquid nitrogen. Cryosections (10 μm thick) were stored at −80 °C until use. Prior to staining, sections were washed once in PBS for 10 min and twice in 0.1% Triton X-100/PBS for 10 min each. Blocking was performed using 2.5% normal donkey serum and 2.5% normal goat serum in 0.1% Triton X-100/PBS for 1 h at room temperature. Sections were incubated with primary antibodies overnight at 4 °C and subsequently with Alexa Fluor-conjugated secondary antibodies (Thermo Fisher Scientific) for 1 h at room temperature. For PNA lectin and phalloidin staining, FITC-conjugated *Arachis hypogaea* lectin (1:1000, Sigma-Aldrich, St. Louis, MO, USA), L7381) and Alexa Fluor 647-conjugated phalloidin (1:1000, Thermo Fisher Scientific, A2287) were used, respectively. TUNEL staining was performed using the MEBSTAIN Apoptosis TUNEL Kit Direct (MBL, Tokyo, Japan, 8445) to detect apoptotic cells. Nuclei were counterstained with DAPI for 30 min at room temperature. Imaging was performed using a Leica TCS SP8 confocal microscope, and images were processed using LAS X software (version 2, Leica Microsystems, Vienna, Austria). Laser power and exposure settings were optimized for each experiment but kept constant during acquisition to ensure comparability across samples. Image brightness was adjusted linearly within a consistent dynamic range using Fiji software (NIH). For Fig. 6d, cell quantification was performed using Aivia software (Leica). Statistical analyses and graph generation were performed using Microsoft Excel, except for the AVNOVA test, which was performed in R.

Volume electron microscopy (array tomography)

Immediately following euthanasia, testes were dissected from animals, immersed in half-strength Karnovsky fixative (2% paraformaldehyde, 2.5% glutaraldehyde in 0.1 M phosphate buffer, pH 7.3), bisected in fixative, and fixed for 48 h. The tissue was post-fixed with 1% osmium tetroxide in buffer, dehydrated in a graded ethanol series, and embedded in EPON 812 resin (Tabb, Berks, UK). After trimming to a 0.5 mm square, approximately 600 serial 50 nm ultrathin sections were collected on silicon wafers. Sections were stained with uranyl acetate and modified Sato's lead solution [45] for 5 min each and subjected to SEM

(JSM-IT800SHL, JEOL, Tokyo, Japan) to generate a stack of serial section images. Imaging was conducted at a pixel resolution of 5 nm × 5 nm, with two montaged images per section, each at 7680 × 5760 pixels. After alignment using Stacker Neo (JEOL), 1/2 or 1/4 binning was applied. Three-dimensional ultrastructural visualization and analysis were performed using Amira 2022 and Microscopy Image Browser [46].

Preparation of testis extracts and immunoprecipitation

Wild-type and *MAP7-egfp*^{KI} HeLa cells were lysed in a buffer containing 10 mM Tris-HCl (pH 7.5), 150 mM NaCl, 0.5 mM EDTA, and 0.5% NP-40, supplemented with complete protease inhibitor (Roche Diagnostics, Mannheim, Germany). Testes were harvested from male C57BL/6 wild-type or *Map7-egfp*^{KI} mice at P17–P20, detunicated, and homogenized in the same lysis buffer with protease inhibitors. Lysates were cleared by centrifugation at 100,000 × *g* for 10 min at 4 °C. To reduce nonspecific interactions, supernatants were precleared through incubation with control magnetic agarose beads (ChromoTek) for 1 h at 4 °C with gentle rotation. The resulting supernatants were used as input material for immunoprecipitation.

To isolate Map7/MAP7-EGFP^{KI} complexes, GFP-Trap magnetic agarose beads (50 µL; ChromoTek) were added to the lysates. After incubation, the beads were washed thoroughly with lysis buffer, and bound proteins were eluted with 40 µL of elution buffer (100 mM Glycine-HCl, pH 2.5, 150 mM NaCl) and neutralized with 4 µL of 1 M Tris-HCl (pH 8.0). Eluted samples were separated by SDS–PAGE, transferred to PVDF membranes (Millipore), and analyzed by immunoblotting using specific antibodies. Detection was performed using ECL Prime (GE Healthcare, Madison, WI, USA), and signals were visualized using the FUSION Solo imaging system (Vilber Lourmat, Marine, France).

Mass spectrometry

Immunoprecipitated proteins were separated on 4–12% NuPAGE gels (Thermo Fisher Scientific) and electrophoresed until they migrated approximately 1 cm from the loading wells. Gels were stained with SimplyBlue SafeStain (Thermo Fisher Scientific), and protein-containing bands were excised and diced into approximately 1 mm pieces. Gel fragments were subjected to in-gel digestion: proteins were reduced with dithiothreitol (DTT; Thermo Fisher Scientific), alkylated with iodoacetamide (Thermo Fisher Scientific), and digested overnight at 37 °C using trypsin and Lysyl endopeptidase (Promega, Madison, WI, USA) in 40 mM ammonium bicarbonate buffer (pH 8.0).

The generated peptides were analyzed using an Advanced UHPLC system

(ABRME1ichrom Bioscience) coupled to a Q Exactive mass spectrometer (Thermo Fisher Scientific). Raw data were acquired using Xcalibur software (Thermo Fisher Scientific) and processed using Proteome Discoverer version 1.4 (Thermo Fisher Scientific) in combination with Mascot version 2.5 (Matrix Science, Boston, MA, USA). Searches were conducted against the SwissProt database, restricted to entries for *Homo sapiens* or *Mus musculus*. A decoy database comprising randomized or reversed sequences was used to estimate the false discovery rate (FDR), and peptide identification confidence was evaluated using the Percolator algorithm. Peptide-spectrum matches were filtered to maintain a global FDR below 1%, ensuring high-confidence identifications. The complete LC-MS/MS dataset has been deposited in jPOST [47] under the accession numbers PXD066392 (ProteomeXchange) and JPST003958 (jPOST).

scRNA-Seq

Testes were isolated from *Sox9-ires-gfp* and *Sox9-ires-gfp;Map7*$^{-/-}$ mice at P19, or from *Map7*$^{+/-}$ and *Map7*$^{-/-}$ mice at P23. The tissue was finely minced and digested with 1.2 mg/mL type I collagenase (Fujifilm Wako Pure Chemical) at 37 °C for 10 min, followed by centrifugation to collect tissue pellets. Pellets were incubated with Accutase (Innovative Cell Technologies, San Diego, CA, USA) for 5 min at 37 °C. The digestion was terminated by adding DMEM supplemented with 10% FBS, and the resulting cell aggregates were gently dissociated by pipetting. Cell suspensions were sequentially passed through 95 μm and 35 μm strainers (BD Biosciences, Milpitas, CA, USA) to remove debris and large clumps. Cells were pelleted by centrifugation, resuspended in PBS containing 0.1% bovine serum albumin, and sorted using a SH800 cell sorter (SONY, Tokyo, Japan) to exclude dead cells. GFP-positive cells were isolated for Sertoli cell-specific scRNA-Seq. Viable cells were resuspended in DMEM with 10% FBS. Approximately 7,000 single cells were loaded onto a Chromium controller (10x Genomics, Pleasanton, CA, USA) for droplet-based single-cell capture. Libraries were prepared using the Chromium Single Cell 3 Reagent Kits v3 (10x Genomics), following the manufacturer's protocol, and sequenced on an Illumina HiSeq X platform to generate 150 bp paired-end reads. Details on the number of mice used, total cells captured, mean reads per cell, sequencing saturation, number of genes detected per cell, median UMI counts per cell, and total cell numbers before and after quality control are provided in Extended Data Fig. 6b and Extended Data Fig. 9a. Sequencing data have been deposited in the DDBJ Sequence Read Archive under accession number DRR709131, DRR709132, DRR709133, and DRR709134.

Statistical analysis of scRNA-Seq

Raw FASTQ files were processed and mapped to the mouse reference genome (mm10, GENCODE vM23/Ensembl 98) using the Cell Ranger pipeline (version 4.0, 10x Genomics). Subsequent analyses were performed using R (version 3.6.2) within the RStudio environment (version 1.2.1335). Quality control and primary data processing were conducted using the 'Seurat' package (version 3.2.2) in R [48 49]. Cells expressing fewer than 200 genes were excluded to eliminate low-quality cells. Datasets were merged and normalized using Seurat's SCTransform function. Dimensionality reduction and clustering were performed using RunUMAP, with clustering based on FindNeighbors and FindClusters functions (default parameters). Differentially expressed genes were identified using FindAllMarkers (only.pos = TRUE, min.pct = 0.25, logfc.threshold = 0.25). FindMarkers was used with default parameters for specific pairwise comparisons.

Sertoli cell populations were isolated based on expression of gonadal supporting cell markers (*Gata4*, *Sox9*, *Kitl*, and *Dhh*). Selected cells were visualized using UMAP plots, and clusters expressing markers of other gonadal lineages or high mitochondrial gene content were excluded. Remaining cells were retained for downstream analysis as Sertoli cells.

Germ cells were selected based on *Ddx4* expression and re-visualized on UMAP plots. Clusters expressing somatic markers or showing high mitochondrial gene content were excluded. The remaining cells were analyzed as germ cells. RNA velocity analysis was performed using the Velocyto package (Python 3.7.3) following default settings [50] and visualized using UMAP embeddings generated by Seurat.

Gene enrichment analysis

Gene enrichment analyses were performed using Metascape [51] with default settings, and results were visualized in Microsoft Excel. To characterize each cluster, we used the top 100 representative genes per cluster.

Statistics

All experiments were repeated at least three times using biological replicates. Data are presented as mean ± standard deviation (S.D.) or, for box-and-whisker plots, as median, first and third quartiles, and 5th–95th percentiles. Statistical comparisons between groups were primarily performed using the Student's *t*-test. A P value <0.05 was considered statistically significant. Z-scores for IP-MS analyses were calculated from Mascot scores. Spearman's correlation coefficients were computed to estimate transcriptional similarity between clusters. P values and adjusted P values (*padj*) during the estimation of Sertoli cell proportions per cluster were

calculated using Fisher's exact test. One-way ANOVA was performed to assess statistical significance during the quantification of round spermatids and pachytene spermatocytes.

Data Availability

The LC-MS/MS and scRNA-Seq datasets generated in this study have been deposited in public repositories. Accession numbers are listed in the Materials and Methods section of the main text.

Acknowledgements

We thank Dr. Nishinakamura for generously providing the MYH9 antibody. We are also grateful to members of our laboratory for their insightful discussions and technical support. This work was partially conducted at the Center for Animal Resources and Development and the Research Facilities of the School of Medicine, Kumamoto University.

Author contributions

K.K. designed the study, performed the majority of the experiments, interpreted the data, and wrote the manuscript. T.F. and N.M. contributed to the initial analysis of *Map7* KO mice. K.O. assisted with array tomography analysis. R.S. contributed to scRNA-Seq analysis. S.F. supported histological analysis. K.Y. and S.U. assisted with scRNA-Seq analyses. N.T. conducted the mass spectrometry analysis. A.N. provided advice on IP-MS analysis. K.A. generated the knock-in mice. K.I. provided technical assistance for mouse testis analyses. All authors discussed the results and reviewed the manuscript.

Funding

This study was funded by the Research Program for the Inter-University Research Network for High Depth Omics and the Joint Usage/Research Program for Developmental Medicine, IMEG, Kumamoto University. Additional support was provided by JSPS KAKENHI (Grant Numbers: 19K06664, 22K06226, 25K09632, JP16H06280 [ABiS], JP22H04922 [ABiS], and JP16H06276 [AdAMS]), the MEXT Promotion of Development of a Joint Usage/Research System Project: Coalition of Universities for Research Excellence (CURE) Program (Grant Number JPMXP1323015486), and grants from the Novartis Foundation for the Promotion of Science, the Mochida Memorial Foundation, the Takeda Science Foundation, and the Uehara Memorial Foundation (to K.K.). Further support was provided by MEXT KAKENHI (JP23H00379, 25H01304), AMED PRIME (21gm6310021h0003), and grants from the Naito Foundation, the Astellas Foundation, and the Takeda Science Foundation (to K.I.).

Conflict of Interest

The authors declare that the research was conducted in the absence of any commercial or financial relationships that could be construed as a potential conflict of interest.

Figure legends

Figure 1. MAP7 exhibits polarized localization to the apical side of microtubule bundles along the apical-basal axis in Sertoli cells.

(**a**) Sections of seminiferous tubules from 8-week-old *Map7-egfp*^{KI} mice were stained for GFP, β-III-tubulin (TUBB3), and DAPI. TUBB3 was used as a Sertoli cell-specific marker. The lower panel shows seminiferous tubules containing step 9–11 spermatids. Scale bar: 50 or 25 μm. (**b**) Sections of seminiferous tubules from 8-week-old *Map7-egfp*^{KI} mice were stained for GFP, acetylated tubulin, and DAPI. The lower panel shows a magnified view of step 9 spermatids. Scale bar: 50, 25, or 10 μm. (**c**) Sections of seminiferous tubules from 8-week-old wild-type mice were stained for MAP7, TUBB3, and DAPI. The lower panel shows seminiferous tubules containing step 9–11 spermatids. Scale bar: 50 or 25 μm.

Figure 2. MAP7 regulates the orientation and morphology of Sertoli cells along the apical-basal axis.

(**a**) Hematoxylin and eosin staining of the sections from testes of the indicated mice (10-, 17-, 21-, 28-, or 35-days old). Biologically independent mice (N = 3) for the indicated genotype were examined. Scale bar: 100 μm. (**b**) The percentage of seminiferous tubules with lumens at the indicated time points was calculated. Data from more than 140 seminiferous tubules from mice (three independent experiments) are indicated and represent the average ± standard deviation (S.D.) (**c**). Array tomography images of seminiferous tubules in mice (10- or 21-day-old). Using a serial-section scanning electron microscope (SEM), 503, 588, 398, or 498 images were obtained at P10 or P21 from *Map7*$^{+/-}$ and *Map7*$^{-/-}$ mice, respectively. Sertoli cells (green), spermatogonia (orange), and spermatocytes (red) were identified based on their nuclear and cellular morphology and adhesion to the basement membrane during the examination of serial-section images. The number represents the ratio of Sertoli cells attached to the basement membrane (upper left, adherent) or Sertoli cell nuclei positioned in the basal layer (lower left, basal nuclei) to the total number of Sertoli cells observed in the stack file (right). The three-dimensional images of Sertoli cells were constructed by manually segmenting serial-section images. Blue or yellow indicates Sertoli cells or basement membrane, respectively. T and L represent views from the transverse and longitudinal axes of the seminiferous tubules, respectively. Scale bar: 10 μm. (**d**) The orientation of Sertoli cell nuclei along the apical–basal axis and actin remodeling on the apical side were analyzed in mice (10- or 17-day-old). To view the orientation of Sertoli cell nuclei along the apical–basal axis, seminiferous tubules were

stained for DAPI and SOX9, allowing detection of Sertoli cell nuclei. Seminiferous tubule morphology was visualized with phalloidin (F-actin) staining. Scale bar: 25 μm. (**e**) The percentage of $Sox9^{+}$ Sertoli cells per cell layer at P10 and P17 was calculated. Data were obtained from more than 145 $SOX9^{+}$ Sertoli cells in mice (using more than ten images acquired after three independent experiments), presented as mean ± S.D. Statistical significance between data points was assessed using Student's *t*-test. *, $P<2.20\times10^{-4}$. (**f**) The germ-independent polarity formation of Sertoli cells was analyzed by eliminating the male germ cell lineage with busulfan treatment. At 28 days old, mice were intraperitoneally injected with busulfan (45 μg/g) and dissected six weeks later for observation using hematoxylin and eosin staining. Biologically independent mice (N = 4) of the specified genotype were examined. Scale bar: 50 μm.

Figure 3. MAP7 facilitates microtubule remodeling, but not microtubule stabilization, to establish Sertoli cell polarity.

(**a**) Seminiferous tubule sections derived from *Map7-egfp*^{KI} mice (10- or 17-day-old) were stained for GFP, TUBB3, phalloidin (F-actin), and DAPI. Scale bar: 50 μm. (**b**) The direction and stabilization of microtubule bundles in Sertoli cells were analyzed using three-dimensional projection images from mice (17-day-old). Seminiferous tubule sections were stained with TUBB3 (β-III-tubulin), phalloidin (F-actin), β-catenin, and DAPI. Notably, the proportion of seminiferous tubules in *Map7*$^{-/-}$ mice where TUBB3, F-actin, and β-catenin were abnormally accumulated on the inner side of the tubules was consistent with the proportion of tubules lacking lumen formation, as shown in Fig. 2a, b. Scale bar: 50 or 25 μm. (**c**) Tight junction formation between Sertoli cells adhering to the basement membrane was analyzed in 10- or 21-day-old mice and visualized as electron-dense structures in SEM images. The black arrow indicates the cell boundary at P10, whereas magenta and blue arrows indicate tight and adherens junctions, respectively. Scale bar: 1 μm. (**d**) Tight junction formation of Sertoli cells was analyzed using three-dimensional projection images in mice (17-day-old). The percentage of seminiferous tubules with ectopic ZO-1 was calculated. Data are from more than 45 seminiferous tubules in mice (three independent experiments), and represent the average ± S.D. Statistical significance is indicated by $P<0.002$ (Student's *t*-test). Scale bar: 25 μm.

Figure 4. MAP7 mediates cytoskeletal cross-talk by forming a complex with actomyosin components.

(**a**) Immunoprecipitation-mass spectrometry (IP-MS) analysis using *MAP7-egfp*^{KI} HeLa cells. Lysates from wild-type HeLa cells were used as a negative control for immunoprecipitation (IP). Volcano plot of proteins identified in both control and Map7-EGFP^{KI} IP samples, excluding keratin and immunoglobulin-derived proteins. Protein quantification was performed based on Mascot scores. Proteins with a log□ fold change (Map7-EGFP^{KI} IP / Control IP) > 1 and a z-score > 2 are highlighted in red. Proteins, such as MVP, MAP7, and KIF5B, which had high scores on both metrics, are labeled. (**b**) IP-MS analysis using testes from P17–20 *Map7-egfp*^{KI} mice. Lysates from age-matched wild-type testes were used as the negative control. Volcano plot of proteins identified in both control and MAP7-EGFP^{KI} IP samples, with keratin and immunoglobulin-derived proteins excluded. Proteins with a log□ fold change > 1 and z-score > 2 are marked in red. Proteins, such as MAP7, MYH9, MYH10, and KIF5B, which had high scores on both metrics, are labeled. (**c**) A Venn diagram comparing interacting proteins identified in *MAP7-egfp*^{KI} HeLa cells and P17–20 *Map7-egfp*^{KI} testes. Ten common interactors were identified, including known MAP7-binding partners, such as KIF5B and its light chain KLC2, as well as TUBB4B, a beta-tubulin isoform. (**d**) Enrichment analysis using Metascape was performed on 22 Sertoli-specific MAP7-interacting proteins identified exclusively in P17–20 *Map7-egfp*^{KI} testes. (**e**) Cytoskeleton-associated proteins that were below the detection limit in the Control-IP are highlighted. Sertoli cell-specific proteins are indicated in red. Proteins are classified based on their association with microtubules (MT), actin filaments (AF), or intermediate filaments (IF). The Mascot score represents a confidence metric generated by the Mascot search engine, indicating the probability that the observed peptide matches correspond to a specific protein in the database. Peptide-spectrum match (PSM) denotes the number of spectra that confidently match a given peptide, reflecting the reliability of peptide identification. (**f**) Localization of MYH9 in Sertoli cells. Testes from 17-day-old mice were subjected to immunofluorescence analysis. Cross-sections of seminiferous tubules were stained with antibodies against TUBB3, MYH9, and phalloidin for F-actin, along with DAPI for nuclear visualization. Regions labeled 1 and 2 correspond to magnified views shown in the respective panels. Scale bar: 50 or 25□μm.

Figure 5. Functional differentiation of Sertoli cells is largely preserved in the absence of MAP7.

(**a**) UMAP visualization of transcriptomic profiles from Sertoli cells isolated from P19 testes of specified genotypes. The control was prepared by pooling testes from one wild-type and two *Map7*$^{+/-}$ littermate mice. Testes from *Map7*$^{-/-}$ littermates were used for comparison. Clusters

were defined based on distinct gene expression patterns. (**b**) Violin plots showing the expression of cluster-specific gene sets, selected from the top 100 differentially expressed genes in each cluster, as identified by Metascape enrichment analysis. (**c**) Spearman's correlation coefficients between clusters represent transcriptional similarity. A minimum spanning tree (MST) constructed from these coefficients illustrates putative transitions between clusters. (**d**) Proportions of Sertoli cells in each cluster across genotypes. Statistical differences between the control and *Map7*$^{-/-}$ Sertoli cells were assessed using Fisher's exact test; *P* values and adjusted *P* values (padj) are shown.

Figure 6. Sertoli apical domain ensures orderly progression of the pachytene stage during meiosis.

(**a**) Whole-mount immunofluorescence of seminiferous tubules from 8-week-old mice showing GFRα1^{+} spermatogonial stem cells (SSCs). Tubules were stained for GFRα1 and DAPI and imaged from the basal side by z-sectioning. Scale bar, 50 μm. (**b**) Quantification of GFRα1^{+} SSCs per 10^4 μm^2 based on the basal area of seminiferous tubules. Data were collected from 40 tubules per genotype across three independent experiments. (**c**) Immunofluorescence analysis of ZFP541^{+} round spermatids and SYCP3^{+}/ZFP541^{+} pachytene spermatocytes in testis sections from 8-week-old mice. Sections were stained with PNA (acrosome marker), SYCP3, ZFP541, and DAPI. Scale bars, 50 and 25 μm. (**d**) Quantification of ZFP541^{+} round spermatids (RS) and SYCP3^{+}/ZFP541^{+} pachytene spermatocytes (Pachy Sp) per 10^3 μm^2. Data were obtained from 28 images per genotype across three independent experiments. Statistical significance was assessed by one-way ANOVA ($P<0.003$), followed by the Student's *t*-test, with significance indicated as follows: *, $P<4\times10^{-6}$; **, $P<4\times10^{-5}$. (**e**) UMAP visualization of scRNA-Seq transcriptomic profiles from germ cells isolated from 23-day-old testes from specified genotypes. Clusters were defined based on gene expression patterns. Arrows indicate the direction of germ cell differentiation. Spg, Sp, and RS denote spermatogonia, spermatocytes, and round spermatids, respectively. (**f**) Proportions of indicated germ cell types within each cluster in the indicated mice. To further resolve spermatocyte sub-stages, expression levels of sex chromosomal genes (bottom panel) were assessed and visualized as violin plots to assist in stage classification. (**g**) Clustered UMAP representations of specified genotypes (left panel). *Prelid1*, a gene expressed through early pachytene (middle panel), and *Ccna1*, a late pachytene-enriched gene (right panel), were used as molecular markers to classify clusters f–j into early, mid, or late pachytene stages.

References

1. O'Donnell, L., Smith, L.B. & Rebourcet, D. Sertoli cells as key drivers of testis function. *Seminars in cell & developmental biology* **121**, 2-9 (2022).
2. Tanwar, P.S., Kaneko-Tarui, T., Zhang, L. & Teixeira, J.M. Altered LKB1/AMPK/TSC1/TSC2/mTOR signaling causes disruption of Sertoli cell polarity and spermatogenesis. *Human Molecular Genetics* **21**, 4394-4405 (2012).
3. Xiong, Z. *et al.* Raptor directs Sertoli cell cytoskeletal organization and polarity in the mouse testis†. *Biology of Reproduction* **99**, 1289-1302 (2018).
4. Heinrich, A., Bhandary, B., Potter, S.J., Ratner, N. & DeFalco, T. Cdc42 activity in Sertoli cells is essential for maintenance of spermatogenesis. *Cell reports* **37**, 109885 (2021).
5. Heinrich, A., Potter, S.J., Guo, L., Ratner, N. & DeFalco, T. Distinct Roles for Rac1 in Sertoli Cell Function during Testicular Development and Spermatogenesis. *Cell reports* **31**, 107513 (2020).
6. Dunleavy, J.E.M., O'Bryan, M.K., Stanton, P.G. & O'Donnell, L. The cytoskeleton in spermatogenesis. *Reproduction (Cambridge, England)* **157**, R53-R72 (2019).
7. Grove, B.D. & Vogl, A.W. Sertoli cell ectoplasmic specializations: a type of actin-associated adhesion junction? *Journal of Cell Science* **93**, 309-323 (1989).
8. Byers, S., Graham, R., Dai, H.N. & Hoxter, B. Development of Sertoli cell junctional specializations and the distribution of the tight-junction-associated protein ZO-1 in the mouse testis. *American Journal of Anatomy* **191**, 35-47 (1991).
9. Fleming, S.L., Shank, P.R. & Boekelheide, K. γ-Tubulin Overexpression in Sertoli Cells In Vivo: I. Localization to Sites of Spermatid Head Attachment and Alterations in Sertoli Cell Microtubule Distribution1. *Biology of Reproduction* **69**, 310-321 (2003).
10. Fleming, S.L., Shank, P.R. & Boekelheide, K. γ-Tubulin Overexpression in Sertoli Cells In Vivo. II: Retention of Spermatids, Residual Bodies, and Germ Cell Apoptosis1. *Biology of Reproduction* **69**, 322-330 (2003).
11. Wang, F., Zhang, Q., Cao, J., Huang, Q. & Zhu, X. The microtubule plus end-binding protein EB1 is involved in Sertoli cell plasticity in testicular seminiferous tubules. *Experimental Cell Research* **314**, 213-226 (2008).
12. Smith, L.B. *et al.* KATNAL1 Regulation of Sertoli Cell Microtubule Dynamics Is Essential for Spermiogenesis and Male Fertility. *PLOS Genetics* **8**, e1002697 (2012).
13. Roll-Mecak, A. The Tubulin Code in Microtubule Dynamics and Information Encoding. *Dev. Cell* **54**, 7-20. (2020).
14. Cleary, J.M. & Hancock, W.O. Molecular mechanisms underlying microtubule growth dynamics. *Curr. Biol.* **31**, R560-R573. (2021).

15. Barlan, K., Lu, W. & Gelfand, V.I. The microtubule-binding protein ensconsin is an essential cofactor of kinesin-1. *Curr. Biol.* **23**, 317-322. (2013).
16. Metzger, T. *et al.* MAP and kinesin-dependent nuclear positioning is required for skeletal muscle function. *Nature* **484**, 120-124 (2012).
17. Sung, H.H. *et al.* Drosophila ensconsin promotes productive recruitment of Kinesin-1 to microtubules. *Dev. Cell* **15**, 866-876. (2008).
18. Kikuchi, K. *et al.* Map7/7D1 and Dvl form a feedback loop that facilitates microtubule remodeling and Wnt5a signaling. *EMBO Rep.* **19**, e45471. (2018).
19. Tymanskyj, S.R., Yang, B.H., Verhey, K.J. & Ma, L. MAP7 regulates axon morphogenesis by recruiting kinesin-1 to microtubules and modulating organelle transport. *Elife* **7**, e36374. (2018).
20. Hooikaas, P.J. *et al.* MAP7 family proteins regulate kinesin-1 recruitment and activation. *J. Cell Biol.* **218**, 1298-1318. (2019).
21. Kikuchi, K. *et al.* Map7D2 and Map7D1 facilitate microtubule stabilization through distinct mechanisms in neuronal cells. *Life science alliance* **5** (2022).
22. Pan, X. *et al.* MAP7D2 Localizes to the Proximal Axon and Locally Promotes Kinesin-1-Mediated Cargo Transport into the Axon. *Cell Rep.* **26**, 1988-1999. (2019).
23. Adler, A. *et al.* A structural and dynamic visualization of the interaction between MAP7 and microtubules. *Nat Commun* **15**, 1948 (2024).
24. Monroy, B.Y. *et al.* Competition between microtubule-associated proteins directs motor transport. *Nat. Commun.* **9**, 1487. (2018).
25. Monroy, B.Y. *et al.* A Combinatorial MAP Code Dictates Polarized Microtubule Transport. *Dev. Cell* **53**, 60-72.e64. (2020).
26. Fabre-Jonca, N. *et al.* The distribution of murine 115-kDa epithelial microtubule-associated protein (E-MAP-115) during embryogenesis and in adult organs suggests a role in epithelial polarization and differentiation. *Differentiation; research in biological diversity* **63**, 169-180 (1998).
27. Komada, M., McLean, D.J., Griswold, M.D., Russell, L.D. & Soriano, P. E-MAP-115, encoding a microtubule-associated protein, is a retinoic acid-inducible gene required for spermatogenesis. *Genes Dev* **14**, 1332-1342 (2000).
28. Russell, L.D., Bartke, A. & Goh, J.C. Postnatal development of the Sertoli cell barrier, tubular lumen, and cytoskeleton of Sertoli and myoid cells in the rat, and their relationship to tubular fluid secretion and flow. *The American journal of anatomy* **184**, 179-189 (1989).
29. Willems, A. *et al.* Selective ablation of the androgen receptor in mouse sertoli cells affects sertoli cell maturation, barrier formation and cytoskeletal development. *PLoS*

One **5**, e14168 (2010).

30. Bashamboo, A. *et al.* Human Male Infertility Associated with Mutations in NR5A1 Encoding Steroidogenic Factor 1. *The American Journal of Human Genetics* **87**, 505-512 (2010).

31. Ferlin, A. *et al.* Male infertility and androgen receptor gene mutations: clinical features and identification of seven novel mutations. *Clinical Endocrinology* **65**, 606-610 (2006).

32. Flanagan, J.G., Chan, D.C. & Leder, P. Transmembrane form of the kit ligand growth factor is determined by alternative splicing and is missing in the SId mutant. *Cell* **64**, 1025-1035 (1991).

33. Hiort, O. *et al.* Significance of mutations in the androgen receptor gene in males with idiopathic infertility. *The Journal of clinical endocrinology and metabolism* **85**, 2810-2815 (2000).

34. Naughton, C.K., Jain, S., Strickland, A.M., Gupta, A. & Milbrandt, J. Glial Cell-Line Derived Neurotrophic Factor-Mediated RET Signaling Regulates Spermatogonial Stem Cell Fate1. *Biology of Reproduction* **74**, 314-321 (2006).

35. Luaces, J.P., Toro-Urrego, N., Otero-Losada, M. & Capani, F. What do we know about blood-testis barrier? current understanding of its structure and physiology. *Front Cell Dev Biol* **11**, 1114769 (2023).

36. Hofmann, M.C. & McBeath, E. Sertoli Cell-Germ Cell Interactions Within the Niche: Paracrine and Juxtacrine Molecular Communications. *Front Endocrinol (Lausanne)* **13**, 897062 (2022).

37. Oatley, M.J., Racicot, K.E. & Oatley, J.M. Sertoli cells dictate spermatogonial stem cell niches in the mouse testis. *Biol Reprod* **84**, 639-645 (2011).

38. Ishiguro, K.I. *et al.* MEIOSIN Directs the Switch from Mitosis to Meiosis in Mammalian Germ Cells. *Dev Cell* **52**, 429-445.e410 (2020).

39. Watanabe, T., Cheng, E.C., Zhong, M. & Lin, H. Retrotransposons and pseudogenes regulate mRNAs and lncRNAs via the piRNA pathway in the germline. *Genome Res* **25**, 368-380 (2015).

40. Sweeney, C. *et al.* A distinct cyclin A is expressed in germ cells in the mouse. *Development* **122**, 53-64 (1996).

41. Haque, F. *et al.* Non-muscle myosin II deletion in the developing kidney causes ureter-bladder misconnection and apical extrusion of the nephric duct lineage epithelia. *Developmental Biology* **427**, 121-130 (2017).

42. Du, W. *et al.* Myosin II mediates Shh signals to shape dental epithelia via control of cell adhesion and movement. *PLoS Genet* **20**, e1011326 (2024).

43. Nel-Themaat, L. *et al.* Morphometric analysis of testis cord formation in Sox9-EGFP mice. *Dev Dyn* **238**, 1100-1110 (2009).
44. Sakuma, T., Nakade, S., Sakane, Y., Suzuki, K.T. & Yamamoto, T. MMEJ-assisted gene knock-in using TALENs and CRISPR-Cas9 with the PITCh systems. *Nature protocols* **11**, 118-133 (2016).
45. Takagi, I. *et al.* Penetration and Stainability of Modified Sato's Lead Staining Solution. *Journal of Electron Microscopy* **39**, 67-68 (1990).
46. Belevich, I., Joensuu, M., Kumar, D., Vihinen, H. & Jokitalo, E. Microscopy Image Browser: A Platform for Segmentation and Analysis of Multidimensional Datasets. *PLoS Biol* **14**, e1002340 (2016).
47. Okuda, S. *et al.* jPOST environment accelerates the reuse and reanalysis of public proteome mass spectrometry data. *Nucleic Acids Research* **53**, D462-D467 (2024).
48. Butler, A., Hoffman, P., Smibert, P., Papalexi, E. & Satija, R. Integrating single-cell transcriptomic data across different conditions, technologies, and species. *Nat Biotechnol* **36**, 411-420 (2018).
49. Stuart, T. *et al.* Comprehensive Integration of Single-Cell Data. *Cell* **177**, 1888-1902 e1821 (2019).
50. La Manno, G. *et al.* RNA velocity of single cells. *Nature* **560**, 494-498 (2018).
51. Zhou, Y. *et al.* Metascape provides a biologist-oriented resource for the analysis of systems-level datasets. *Nat Commun* **10**, 1523 (2019).

Kikuchi_Figure 1

a

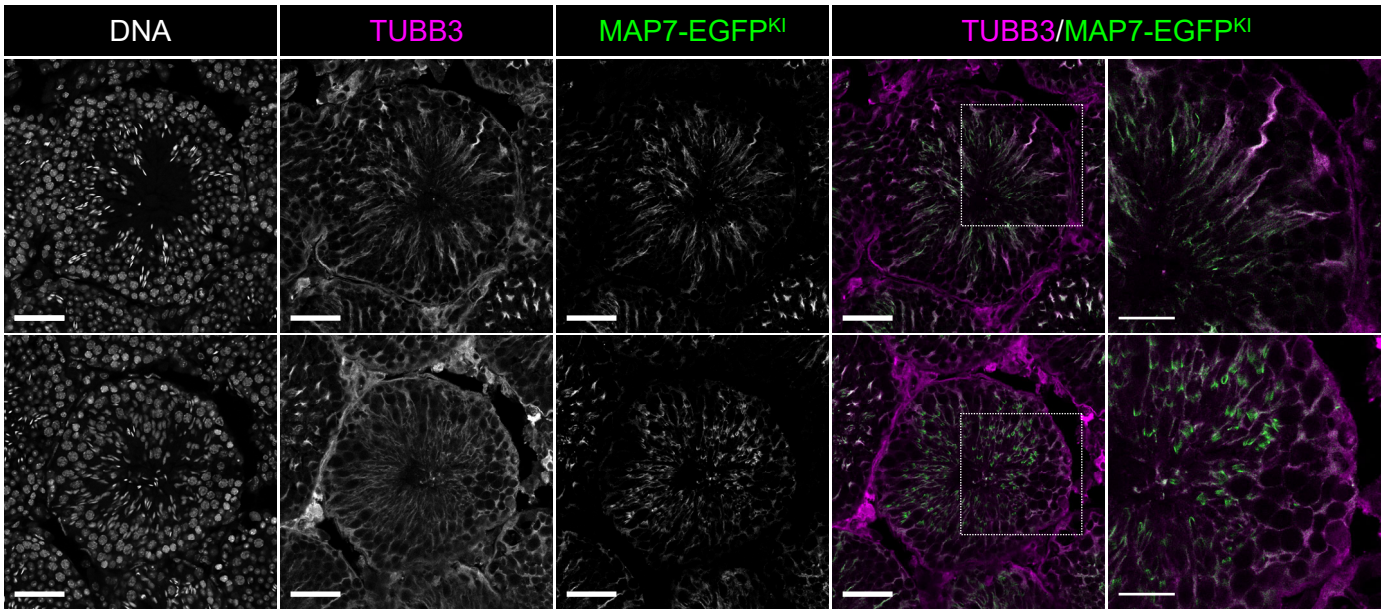

b

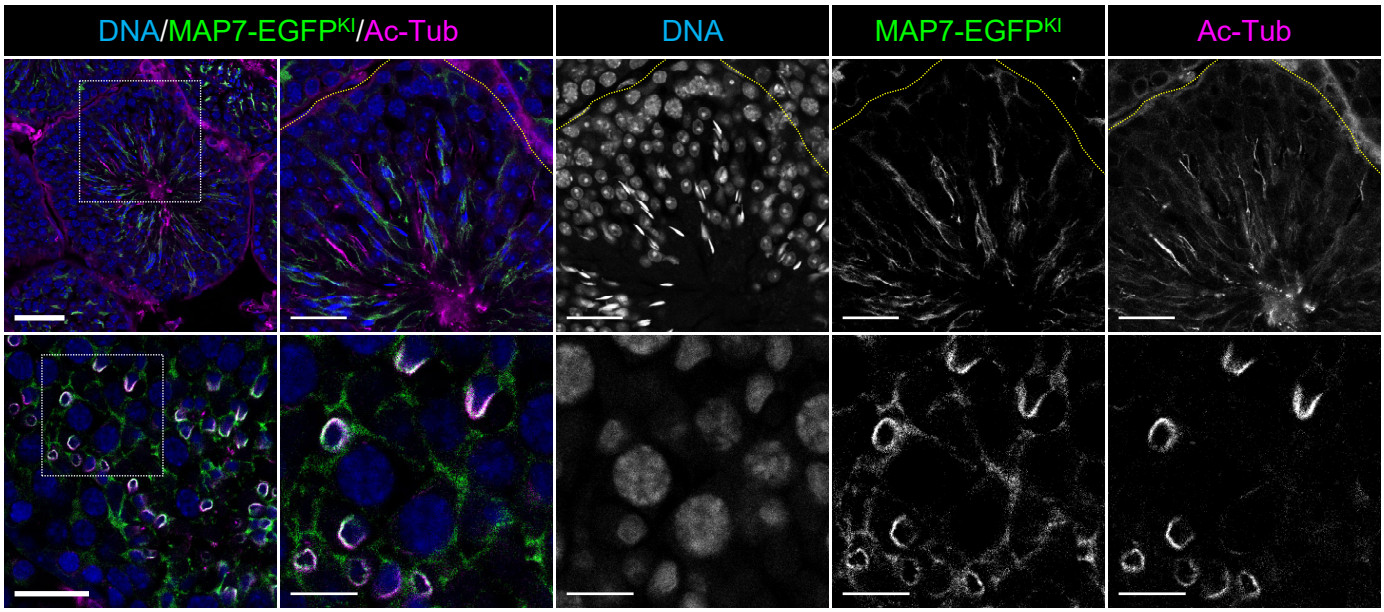

c

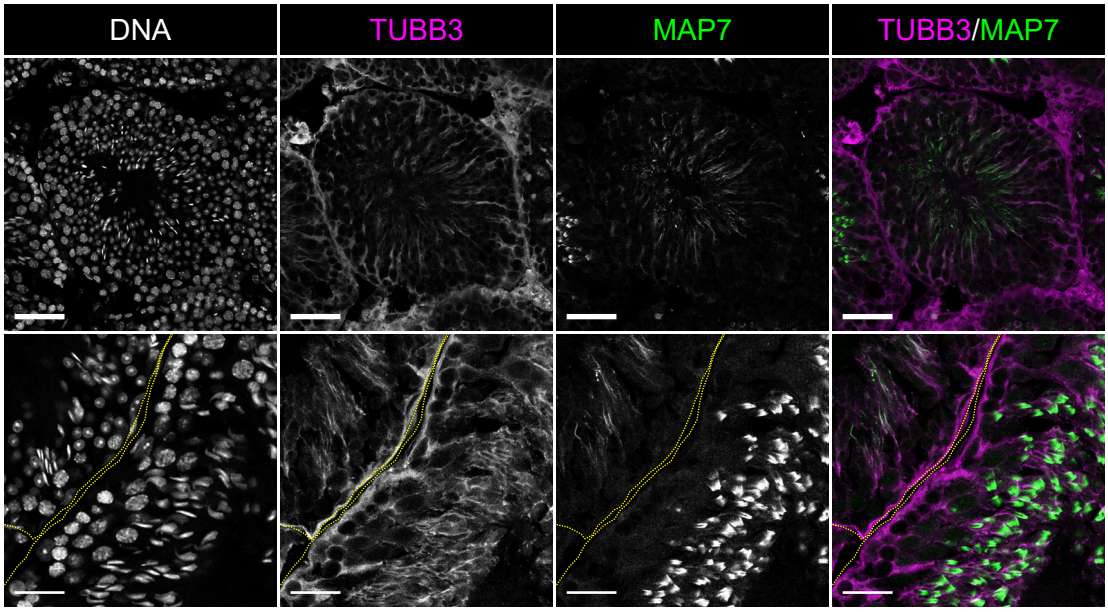

Kikuchi_Figure 2

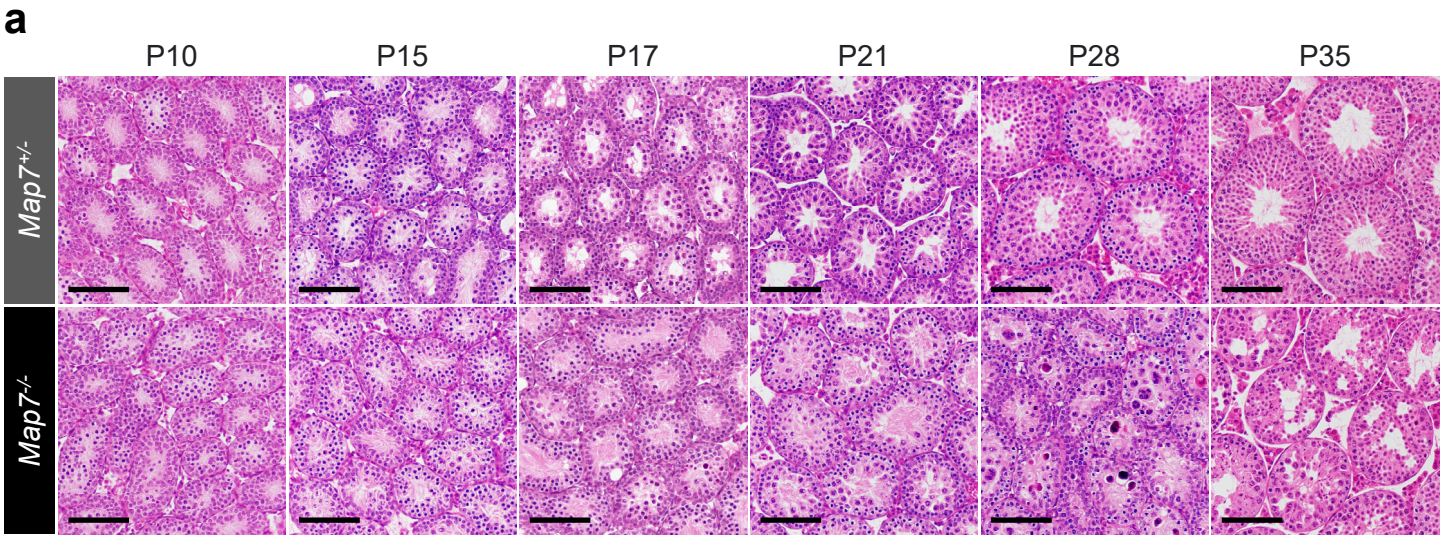

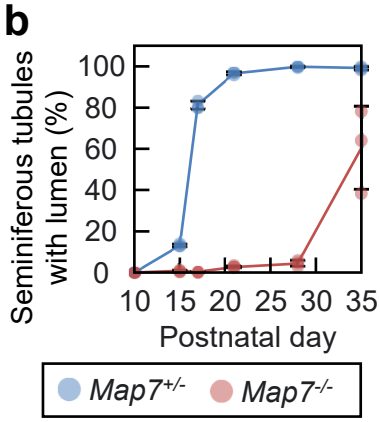

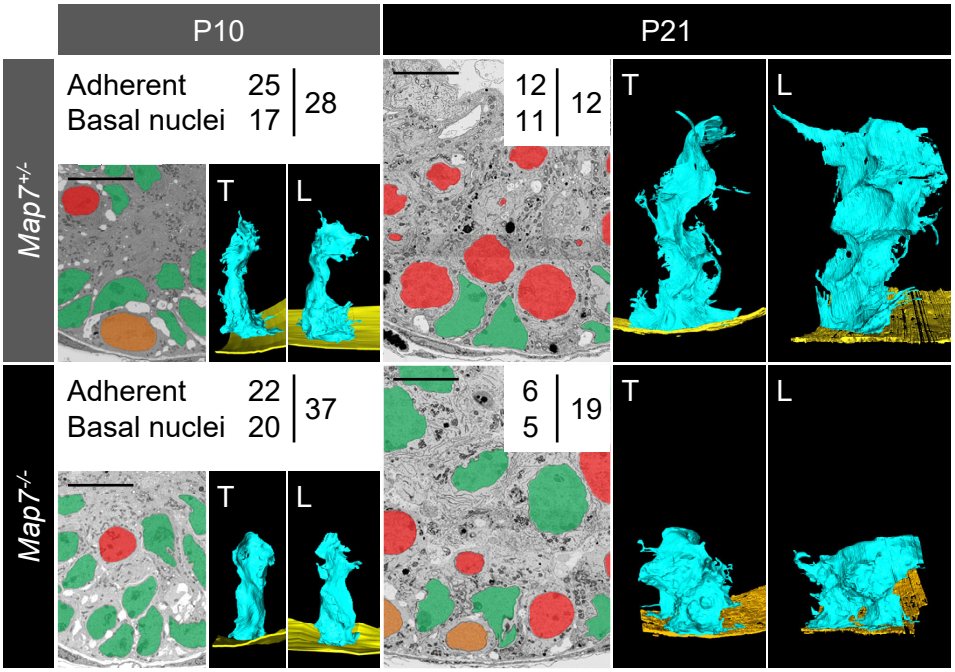

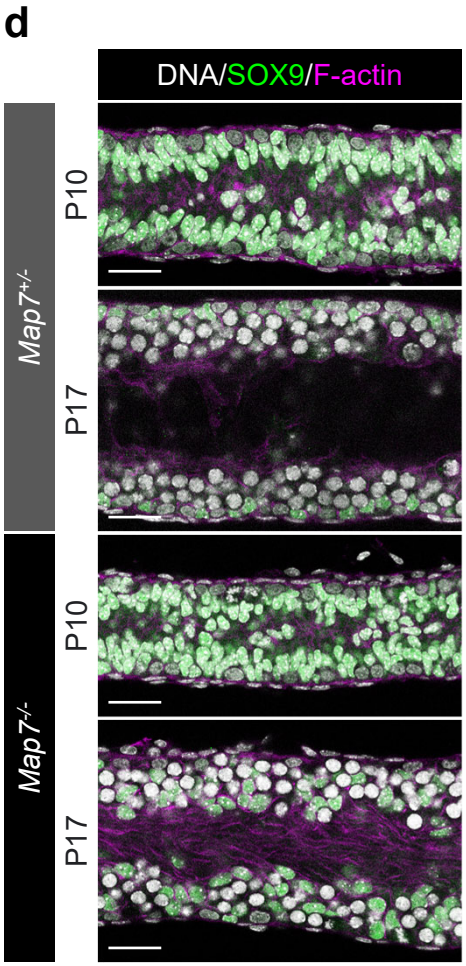

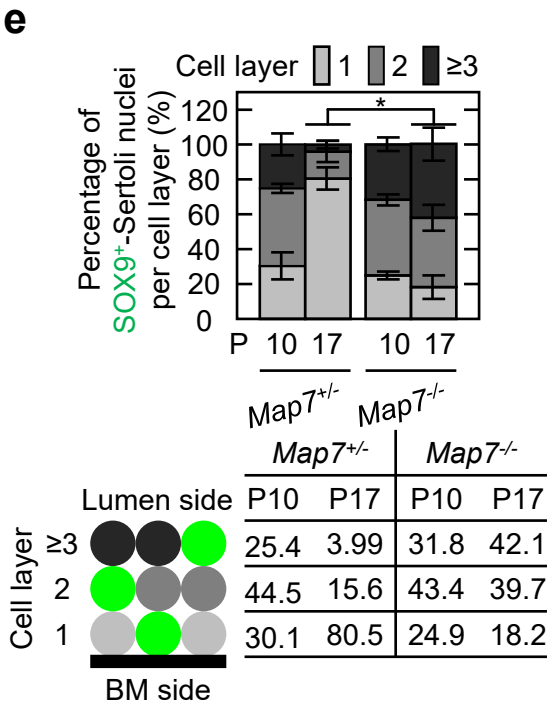

	Map7+/-		Map7-/-	
	P10	P17	P10	P17
≥3	25.4	3.99	31.8	42.1
2	44.5	15.6	43.4	39.7
1	30.1	80.5	24.9	18.2

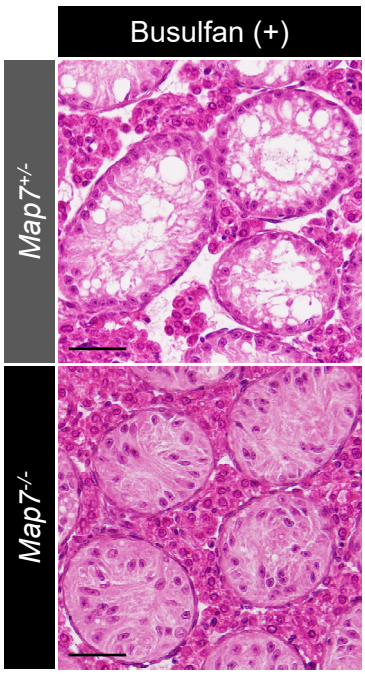

Kikuchi_Figure 3

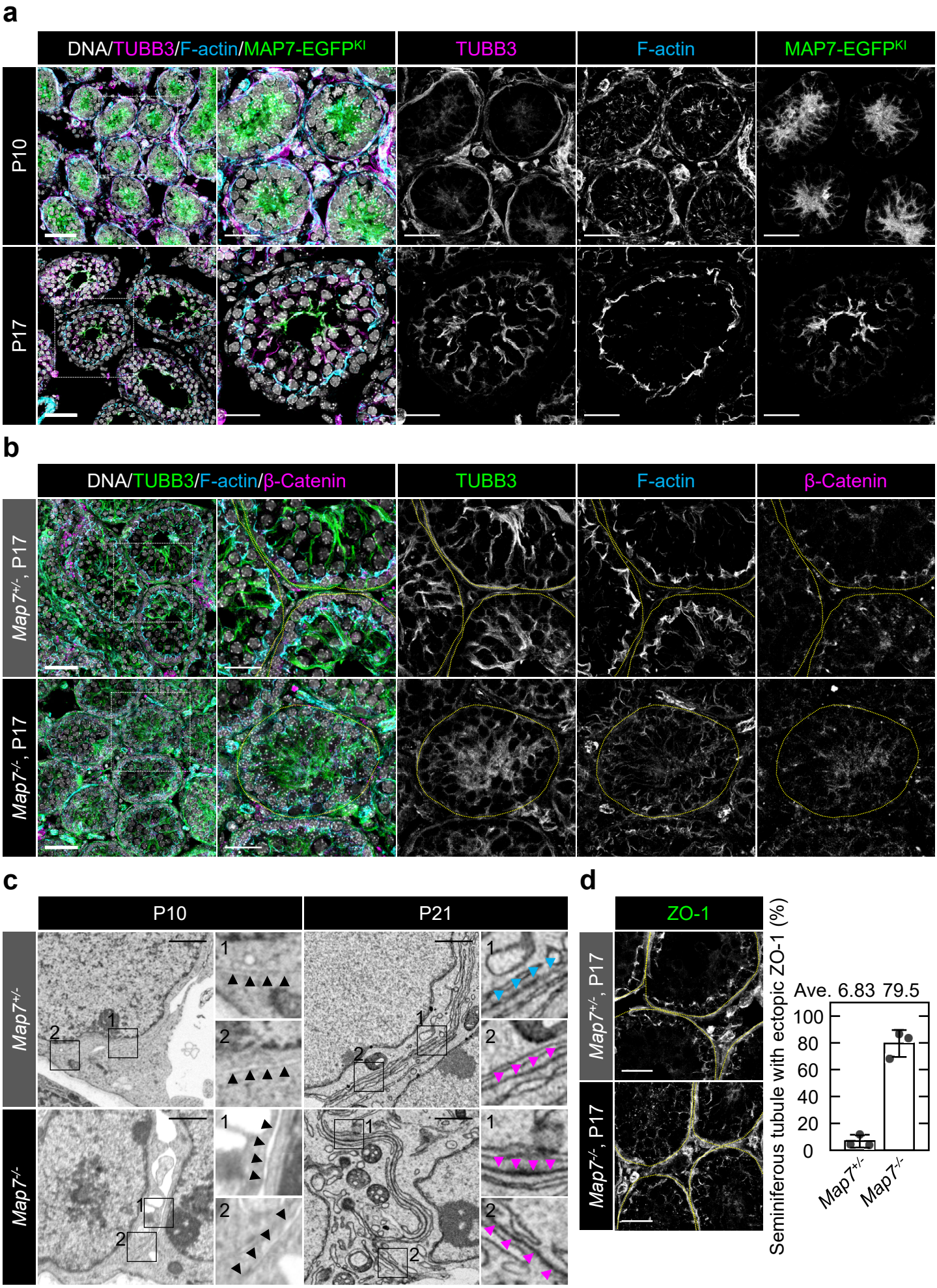

Kikuchi_Figure 4

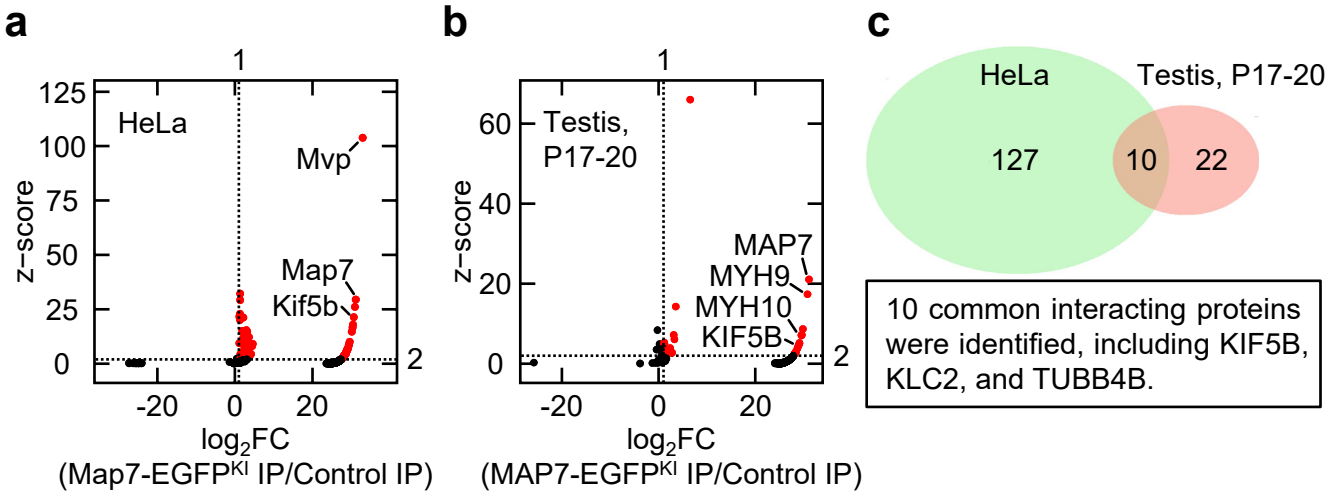

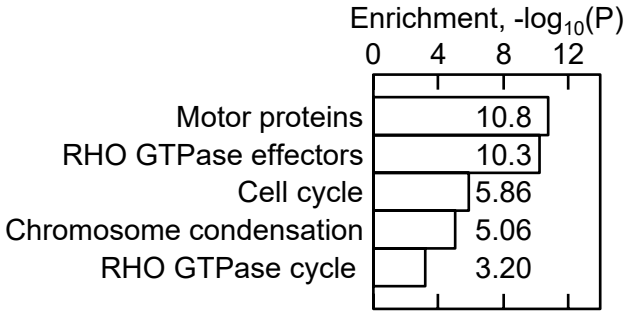

e

	Name	log_2FC	z-score	Mascot score	PSMs
MT	MAP7	31.08339	21.07687	2275.273	172
MT	KIF5B	28.90763	4.437005	503.575	24
MT	TUBB3	28.41413	3.06684	357.6893	18
MT	KLC2	28.0491	2.315854	277.7294	16
AF	MYH9	30.8082	17.36587	1880.151	90
AF	ACTC1	29.83043	8.673716	954.6707	43
AF	MYH10	29.5447	7.062721	783.1432	44
IF	VIM	28.92826	4.505102	510.8255	24

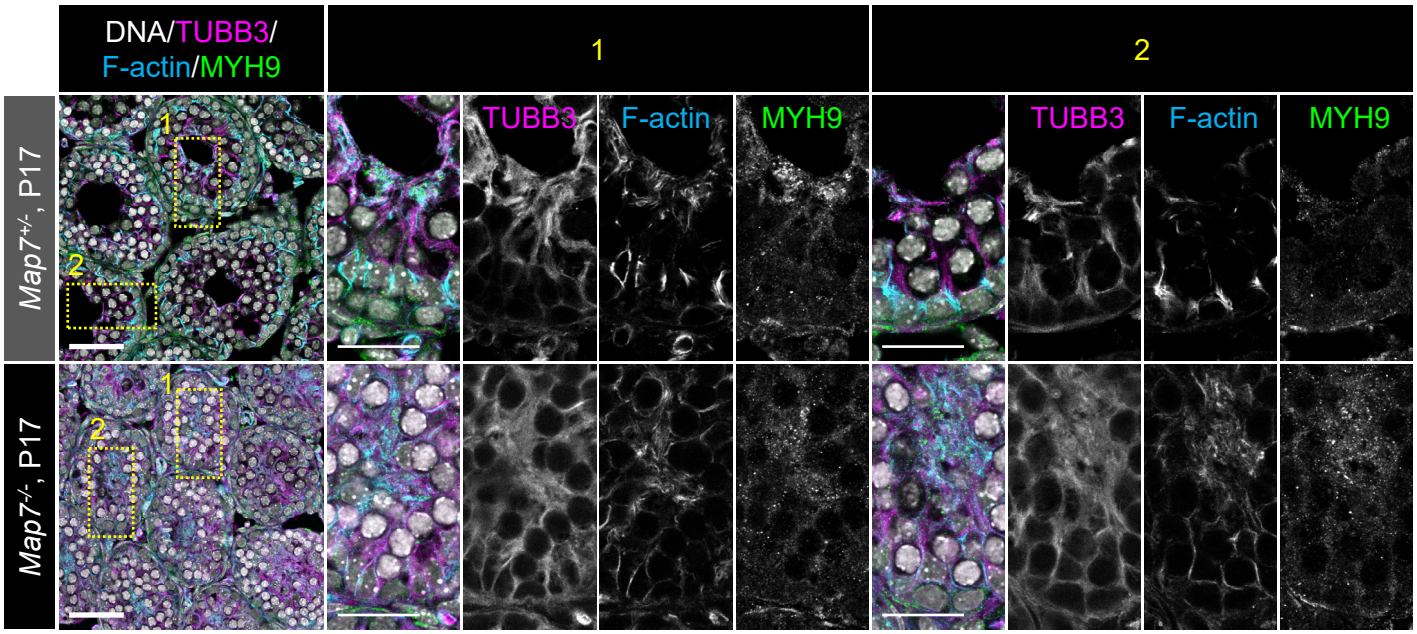

Kikuchi_Figure 5

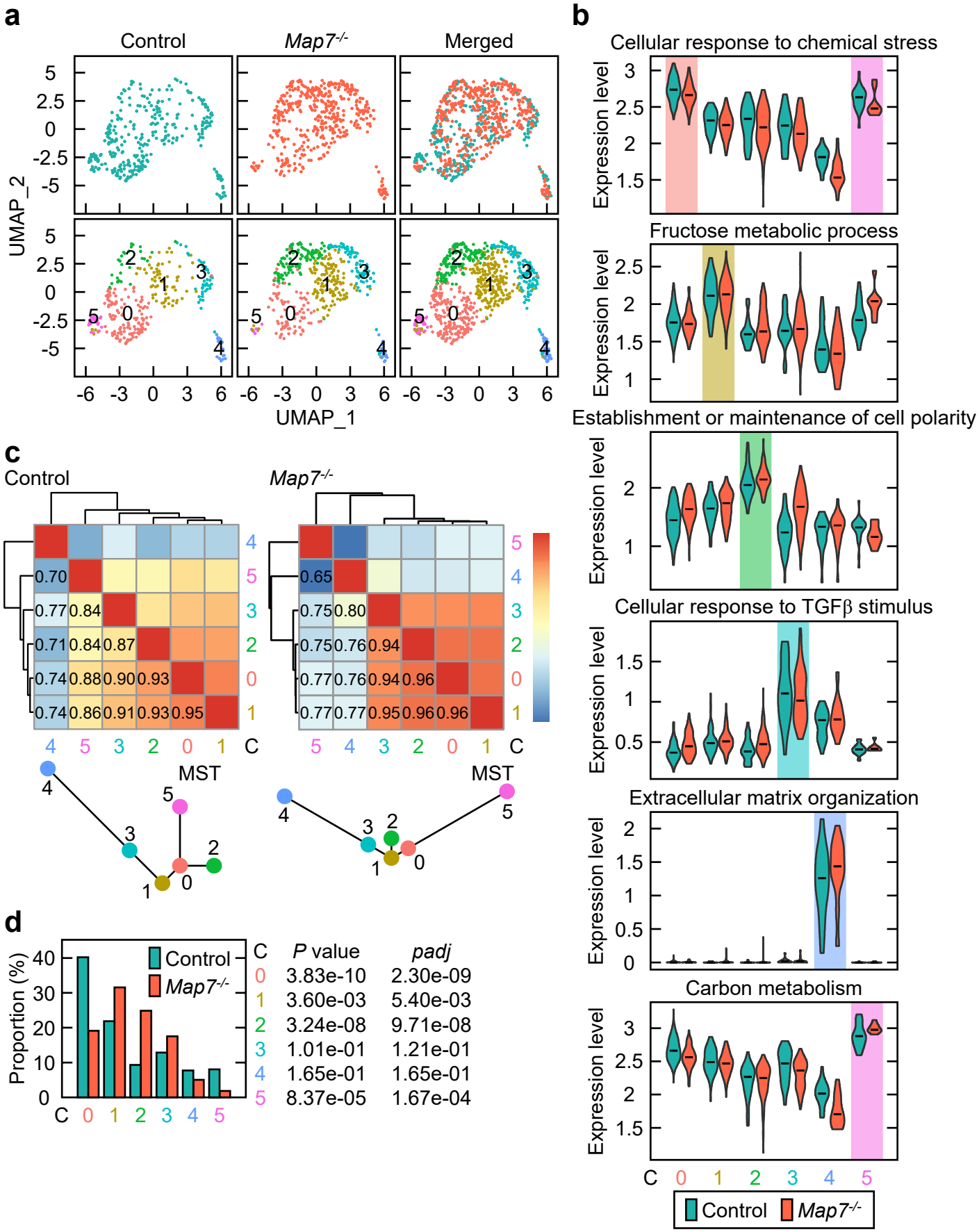

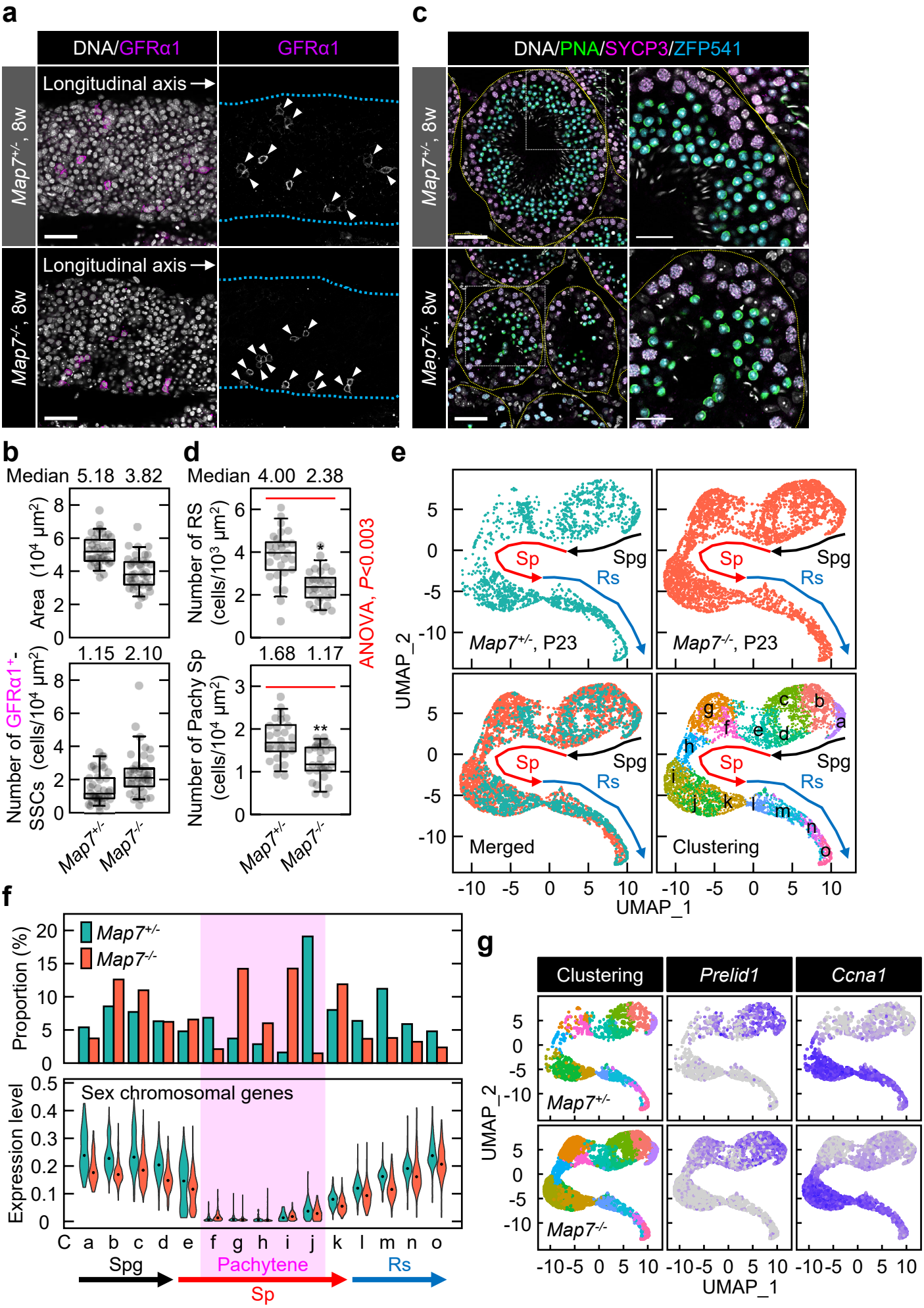
a
DNA/GFRα1
GFRα1
Longitudinal axis
Map7+/-, 8w
Map7-/-, 8w
c
DNA/PNA/SYCP3/ZFP541
b
Median 5.18 3.82
Area (10^4 μm^2)
1.15 2.10
Number of GFRα1+-SSCs (cells/10^4 μm^2)
d
Median 4.00 2.38
Number of RS (cells/10^3 μm^2)
1.68 1.17
Number of Pachy Sp (cells/10^4 μm^2)
ANOVA, P<0.003
e
Sp
Spg
Rs
Map7+/-, P23
Map7-/-, P23
Merged
Clustering
UMAP_1
UMAP_2
f
Proportion (%)
Expression level
Sex chromosomal genes
C a b c d e f g h i j k l m n o
Spg
Pachytene
Rs
Sp
g
Clustering
Prelid1
Ccna1
Map7+/-
Map7-/-
UMAP_1
UMAP_2